Distinct Redox Chemistry in Solid-State Li–S Batteries Induced by Solid Electrolytes

Taehun Kim[1], Jake D. Huang[2], Marvin A. Kraft[1], Johannes Hartel[2], Martin A. Lange[1,2], Wolfgang G. Zeier[1,2]*

1. Institute of Energy Materials and Devices, Helmholtz-Institute Münster (IMD-4), Forschungszentrum Jülich GmbH, 48149 Münster, Germany

2. Institute of Inorganic and Analytical Chemistry, University of Münster, 48149 Münster, Germany

**Corresponding author email: wzeier@uni-muenster.de*

Abstract

The sulfur redox mechanism in solid-state lithium–sulfur (Li–S) batteries remains unclear, as it has been reported to vary under different operating conditions due to sluggish reaction kinetics. Herein, we investigate sulfur reactions in solid-state batteries using solid electrolytes with high ionic conductivities to mitigate kinetic limitations. A solid-state Li–S cell employing $Li_{5.5}PS_{4.5}Cl_{1.5}$ exhibits an asymmetric voltage profile at 25 °C, with two voltage plateaus during discharge and poorly separated oxidation reactions during charge. *Ex situ* X-ray absorption spectroscopy (XAS) elucidates that these poorly separated oxidation reactions consist of overlapping conversion reactions, in contrast to the clearly distinguishable two-step conversion from S_8 to Li_2S via Li_2S_x during discharge. In addition, *operando* impedance evolution, analyzed using a combined distribution of relaxation times (DRT) and distribution of phasances (DOP) model, reveals distinct relaxation processes during discharge and charge that arise from differences in the transport properties of the reaction products. This work demonstrates an intrinsic asymmetric sulfur redox mechanism in solid-state batteries that is difficult to resolve by conventional electrochemical measurements alone but can be clarified by combining XAS with impedance analysis using the DRT-DOP model.

1. Introduction

Lithium–sulfur (Li–S) batteries have garnered extensive attention due to the high specific capacity (1675 mA h g^{-1}), earth-abundance, and low cost of sulfur.[1,2] Nevertheless, the development of conventional liquid electrolyte-based Li–S batteries has been hindered by severe performance degradation arising from the formation of soluble lithium polysulfide species (Li_2S_x, $4 \leq x \leq 8$) and the associated shuttle effect.[3,4] Solid-state Li–S batteries have been proposed as a solution to the shuttle issue, as solid electrolytes (SE) inherently prevent polysulfide dissolution.[5] Despite this promising aspect, the sulfur redox mechanism in solid-state batteries (SSB) remains poorly understood due to the absence of dissolved long-chain lithium polysulfides.

In conventional liquid electrolyte-based Li–S batteries, the sulfur redox reaction undergoes solid–liquid–solid conversion. Solid-phase sulfur is first reduced to long-chain lithium polysulfides dissolved in the liquid electrolyte, and the polysulfides are subsequently precipitated out of the liquid phase as insoluble Li_2S_2 and Li_2S, giving rise to two voltage plateaus.[6] In contrast, such solid–liquid conversion is physically impossible in SSB, leaving the formation of lithium polysulfides and their species unclear. A few studies have investigated the solid–solid conversion pathway in SSB. For instance, a symmetric sulfur conversion reaction from S_8 to Li_2S via a Li_2S_2 intermediate has been reported at 25 °C, with voltage profiles exhibiting a single voltage plateau during both discharge and charge.[7] However, operation at elevated temperatures induces an asymmetric discharge–charge profile, in which two voltage plateaus are observed during discharge, whereas only a single voltage plateau appears during charge, suggesting an asymmetric reaction pathway under enhanced kinetics.[8] Gu *et al.* demonstrated that, at high temperatures, sulfur is reduced from S_8 to Li_2S_4 and subsequently to Li_2S during discharge, while direct conversion of Li_2S to S_8 occurs during charge.[9] These distinct sulfur redox behaviors under different cycling conditions highlight the importance of studying solid-state Li–S batteries under conditions where reaction kinetics are not the limiting factor.

Solid-state Li–S batteries show a considerably higher overpotential than conventional liquid electrolyte-based Li–S batteries.[10] While differences in the reaction pathway contribute to the high overpotential, the highly tortuous conduction pathways in SSB impede the conversion reactions and can further alter the overall reaction mechanism.[11] Unlike flowable liquid electrolytes with good wettability, SE require a homogeneous microstructural architecture to enable ionic percolation. This percolation network can be readily disrupted by the electronically and ionically insulating nature of sulfur.[12] While both ionic and electronic tortuosity factors in solid-state Li–S batteries are high, the ionic transport exhibits a higher tortuosity and acts as a bottleneck.[11]

Therefore, mechanical ball milling is a common method to prepare sulfur composite cathode.[13] Ball milling reduces the particle size of cathode components and increases the interfacial contact area between sulfur and the SE, thereby improving the ionic percolation pathways within the composite.[14] However, despite these advantages, the crystallinity and ionic conductivity are substantially decreased upon the ball-milling process.[15–17] Under harsh milling conditions, the ionic conductivity can decrease by approximately one order of magnitude.[15,17] Considering the high ionic tortuosity in SSB and the conductivity decrease induced by ball milling, the use of highly conductive SE is needed to investigate solid-state Li–S batteries under practical operating conditions with favorable reaction kinetics.

In this work, we investigate the reactions of sulfur in SSB using two chemically different but highly conductive SE, $Li_{5.5}PS_{4.5}Cl_{1.5}$ and Li_6PSe_5Br. The solid-state Li–S cell employing $Li_{5.5}PS_{4.5}Cl_{1.5}$ delivers 81% of the theoretical capacity and exhibits an asymmetric redox behavior in the voltage profiles and the differential capacity (dQ/dV) curves at 25 °C, enabled by the high ionic conductivity of $Li_{5.5}PS_{4.5}Cl_{1.5}$. *Ex situ* S K-edge X-ray absorption spectroscopy (XAS) reveals the asymmetric redox pathway, in which sulfur undergoes a two-step conversion from S_8 to Li_2S_x and subsequently to Li_2S during discharge, whereas Li_2S is converted back to Li_2S_x and then to S_8 through overlapping conversion reactions during charge. In order to trace the evolution of electrochemical processes, *operando* time- and frequency- domain impedance spectroscopy is performed, and the collected impedance data are analyzed using a combined distribution of relaxation times (DRT) and distribution of phasances (DOP) model.[18] The DRT-DOP indicates that ionically and electronically insulating reaction product S_8 impedes electrochemical processes during charge more considerably than the discharge intermediate and product, Li_2S_x and Li_2S. In contrast, a composite cathode prepared with sulfur and Li_6PSe_5Br exhibits a distinctly different electrochemical behavior. The quasi open-circuit voltage (QOCV) curves show two redox couples during discharge and charge. To further examine this behavior, *ex situ* XAS, X-ray photoelectron spectroscopy (XPS), X-ray diffraction (XRD) and Raman spectroscopy are used. Substantial changes occur in the PSe_4^{3-} tetrahedra, the oxidation state of sulfur, and the structure of Li_6PSe_5Br, indicating that planetary ball milling, which is necessary for the Li–S cathode preparation, induces an unintended Se – S exchange reaction between sulfur and Li_6PSe_5Br. Amorphous selenium is formed by this reaction, and both the resulting selenium and excess unreacted sulfur are electrochemically active during cycling, as characterized by *ex situ* XAS and XPS. This work demonstrates the intrinsic asymmetric sulfur redox pathway in SSB and its influence on the electrochemical processes during cycling. Moreover, the Se – S exchange reaction reveals the significance of both SE choice and the essential ball-milling process in

determining chalcogen chemistries. These findings provide insights into the intrinsic limitations of solid-state Li–S batteries and the approaches required to improve their performance.

2. Experimental Section

Synthesis

Precursors and SE were handled in an Ar-filled glove box to avoid air exposure. Lithium sulfide (Sigma-Aldrich, 99.98%), lithium selenide, red phosphorus (Thermo Fisher, 99.999%), selenium (Thermo Fisher, 99.5%), phosphorus pentasulfide (Sigma-Aldrich, 99%), lithium chloride (Sigma-Aldrich, 99%), and lithium bromide (Alfa Aesar, 99%) were mixed in stoichiometric ratios corresponding to each SE. The powders were hand-ground using an agate mortar and pestle and pressed into pellets. The pellets were then sealed under vacuum in carbon-coated ampoules, which were vacuum-dried at 800 °C for 2 h prior to use. The ampoule containing precursors for $Li_{5.5}PS_{4.5}Cl_{1.5}$ was heated to 450 °C at 100 °C h^{-1} in a tube furnace and annealed at the same temperature for 72 h, followed by natural cooling. The annealed pellets were hand-ground and subjected again to the same pressing and annealing process. The ampoules containing precursors for Li_6PSe_5Br and Li_6PS_5Br were heated to 550 °C at 100 °C h^{-1} and annealed at the same temperature for 2 weeks, followed by liquid-nitrogen quenching to obtain a highly disordered phase which offers high ionic conductivity.[19] All obtained SE pellets were hand-ground.

The precursor lithium selenide was prepared using a stoichiometric amount of selenium powder and metallic lithium (abcr, 99.8%) by gas-phase reaction. Metallic lithium was cut into small pieces and placed in a graphite crucible. The crucible and selenium powder were placed in a pre-dried ampoule, separated by small indentations in the ampoule wall. The ampoule was sealed under vacuum and heated to 400 °C at 12 °C h^{-1} in a tube furnace, followed by annealing at the same temperature for 48 h. The annealed sample was allowed to cool naturally and subsequently hand-ground.

Composite preparation

All samples were handled under an Ar atmosphere to avoid air exposure. S–C–$Li_{5.5}PS_{4.5}Cl_{1.5}$ and S–C–Li_6PSe_5Br composites were prepared by a two-step ball-milling process. First, 1.05 g of elemental sulfur (Thermo Fisher, 99.999%) and 0.45 g of carbon black (ECP600JD, ANR Technologies) were ball-milled using a Fritsch PULVERISETTE 7 premium line, resulting in a weight ratio of 7:3. The powders were placed in an 80 mL ZrO_2 cup with 30 g of 5 mm ZrO_2 milling media. Ball milling was performed at 500 rpm for 12 cycles, each consisting of 10 min milling followed by 10 min break. Then, 100 mg of the S–C mixture was ball-milled with 100 mg of $Li_{5.5}PS_{4.5}Cl_{1.5}$ or 200 mg of Li_6PSe_5Br to account for the difference in SE mass density. Ball

milling was conducted using the same method used for the S–C mixture preparation, except that the number of milling cycles was increased to 24.

Se–C–$Li_{5.5}PS_{4.5}Cl_{1.5}$ and Se–C–Li_6PS_5Br composite were also prepared by a two-step ball-milling process. The ball-milling conditions were the same as those used for S–C–$Li_{5.5}PS_{4.5}Cl_{1.5}$ and S–C–Li_6PSe_5Br composites. For the Se–C–$Li_{5.5}PS_{4.5}Cl_{1.5}$ composite, 1.278 g of selenium powder and 0.222 g of carbon black were ball-milled. Then, 202.4 mg of the Se–C mixture was ball-milled with 100 mg of $Li_{5.5}PS_{4.5}Cl_{1.5}$. For the Se–C–Li_6PS_5Br composite, 1.242 g of selenium powder and 0.258 g of carbon black were ball-milled. Then, 181.2 mg of the Se–C mixture was ball-milled with 118.8 mg of Li_6PS_5Br.

The C–$Li_{5.5}PS_{4.5}Cl_{1.5}$ composite was prepared by ball milling 20 mg of carbon black with 180 mg of $Li_{5.5}PS_{4.5}Cl_{1.5}$ under the same conditions used for the S–C–$Li_{5.5}PS_{4.5}Cl_{1.5}$ composite. For the preparation of the S–Li_6PSe_5Br composite, 70 mg of sulfur and 200 mg of Li_6PSe_5Br was ball-milled under the same conditions used for the S–C–Li_6PSe_5Br composite.

Cell fabrication

Half-cells were fabricated using a customized press-cell setup (10 mm diameter) reported elsewhere.[20] 90 mg of $Li_{5.5}PS_{4.5}Cl_{1.5}$ was manually pressed as a separator layer using a screw press. For the S–C–$Li_{5.5}PS_{4.5}Cl_{1.5}$ and S–C–Li_6PSe_5Br half-cells, 9 mg of S–C–$Li_{5.5}PS_{4.5}Cl_{1.5}$ (mass ratio S:C:SE = 7:3:10) or 13.5 mg of S–C–Li_6PSe_5Br (mass ratio S:C:SE = 7:3:20) composite was evenly distributed onto one side of the separator layer, resulting in an areal capacity of 6.72 mA h cm^{-2} calculated based on the theoretical capacity of sulfur (1675 mA h g^{-1}). For the Se–C–$Li_{5.5}PS_{4.5}Cl_{1.5}$ and Se–C–Li_6PS_5Br half-cells, 13.6 mg of Se–C–$Li_{5.5}PS_{4.5}Cl_{1.5}$ (mass ratio Se:C:SE = 17.2:3:10) or 15.5 mg of Se–C–Li_6PS_5Br (mass ratio Se:C:SE = 50:10.4:39.6) composite was used to achieve the same areal capacity, calculated based on the theoretical capacity of selenium. For the C–$Li_{5.5}PS_{4.5}Cl_{1.5}$ half-cell, 10 mg of C–$Li_{5.5}PS_{4.5}Cl_{1.5}$ (mass ratio C:SE = 1:9) was used. After distributing composite cathode powders, cathode and separator layers were uniaxially pressed together under a load of 3 tons for 3 min. Indium foil (Haines & Maassen, 99.999%, 100 μm thickness, 9 mm diameter) was attached to the other side of the separator layer, and Li foil (2.0 mg) was stacked on the indium foil to form an In/LiIn anode.

For the In | $Li_{5.5}PS_{4.5}Cl_{1.5}$ | In/LiIn cell, 90 mg of $Li_{5.5}PS_{4.5}Cl_{1.5}$ was manually pressed using a screw press, followed by uniaxial pressing under a load of 3 tons for 3 min. An indium foil (100 μm thickness, 9 mm diameter) was attached to both sides of the separator layer, and 2.0 mg of Li foil was stacked on one side of

the indium foil to form an In/LiIn anode.

All cells were tightly closed using a wrench and placed in a metal frame maintaining a stack pressure of ≈ 50 MPa during electrochemical measurements.

Electrochemical Characterization

S–C–$Li_{5.5}PS_{4.5}Cl_{1.5}$, S–C–Li_6PSe_5Br, and Se–C–Li_6PS_5Br half-cells were discharged and charged using a Maccor Series 4000 in the voltage range from 1.0 to 2.4 V vs In/LiIn at a C-rate of 0.1C, corresponding to an areal current density of 0.672 mA cm^{-2}. Rate performance tests on S–C–Li_6PSe_5Br and Se–C–Li_6PS_5Br half-cells were performed at various current densities of 0.05C (0.336 mA cm^{-2}), 0.1C (0.672 mA cm^{-2}), 0.2C (1.344 mA cm^{-2}), 0.5C (3.358 mA cm^{-2}), and 1C (6.717 mA cm^{-2}) at 25 °C. For the cycling and rate performance tests on S–C–Li_6PSe_5Br and Se–C–Li_6PS_5Br, triplicates of half-cells were evaluated. C–$Li_{5.5}PS_{4.5}Cl_{1.5}$ half-cell was discharged and charged in the same voltage range at an areal current density of 0.498 mA cm^{-2} at 25 °C. The current was determined to match the carbon-based specific current (390.8 mA g_C^{-1}) used for the S–C–$Li_{5.5}PS_{4.5}Cl_{1.5}$ half-cell. Galvanostatic intermittent titration technique (GITT) measurements were conducted on S–C–$Li_{5.5}PS_{4.5}Cl_{1.5}$, Se–C–$Li_{5.5}PS_{4.5}Cl_{1.5}$, and S–C–Li_6PSe_5Br half-cells in the voltage range from 1.0–2.4 V vs In/LiIn with a pulse current of 0.672 mA cm^{-2} for 15 min, followed by relaxation for 10 h at 25 °C.

X-ray absorption spectroscopy

Ex situ samples were discharged/charged to specific depth of discharge/state of charge (DOD/SOC) levels at 0.672 mA cm^{-2} in the voltage range of 1.0–2.4 V vs In/LiIn at 25 °C. The cell configuration and assembly process were the same as those used for electrochemical characterization. Cathodes were carefully retrieved from the cells in an Ar-filled glovebox after discharging/charging. Measurements were performed at the S K-edge in fluorescence yield (FY) mode at beamline B18 of Diamond Light Source. Samples were mounted on a holder in an Ar-filled glove box and transferred to the chamber using an air-tight shuttle. The obtained spectra were processed using an Athena software package.[21]

***Operando* hybrid electrochemical impedance spectroscopy**

S–C–$Li_{5.5}PS_{4.5}Cl_{1.5}$, S–C–Li_6PSe_5Br, and Se–C–Li_6PS_5Br half-cells were discharged and charged at a constant current of 0.1C (0.672 mA cm^{-2}) in the voltage range from 1.0–2.4 V vs In/LiIn using a BioLogic VMP-300 potentiostat at 25 °C. *Operando* impedance spectra were collected during cycling using an

accelerated time- and frequency-domain ("hybrid") measurement technique described previously.[22] Measurements alternated between 60 s intervals of constant current and hybrid impedance measurements, which lasted for approximately 70 s. After each constant current discharge/charge for 60 s, hybrid impedance spectroscopy was conducted. Time-domain measurements probing the frequency range 20 Hz to 10 mHz were carried out by maintaining a DC current of 0.1C while superimposing biphasic current steps of amplitude equivalent to 0.01C for time intervals of 0.16, 1.6, and 16 s, thereafter returning to the 0.1C DC current for 16 s. Subsequently, galvanostatic electrochemical impedance spectroscopy (GEIS) was employed for frequency-domain measurements while maintaining the DC current of 0.1C. The measurements were performed using potentiostatic amplitude selection with an AC root-mean-square excitation amplitude of 7.071 mV, 6 points per frequency decade from 2 MHz to 20 Hz, and 2 cycles per frequency.

The obtained time- and frequency-domain data were jointly transformed into the two-dimensional (2D) distribution of relaxation times (DRT) and distribution of phasances (DOP), allowing impedance and DRT-DOP analysis over the full frequency range 2 MHz to 10 mHz. We employed a self-tuning hierarchical Bayesian model for DRT-DOP fitting. This approach reduces subjective parameter selection and performs favorably relative to methods such as cross-validation, as reported previously.[23] The model uses hierarchical Tikhonov-like regularization to address the ill-posed inversion problem, with weaker regularization applied to the DOP than to the DRT. This allows the DOP to capture constant-phase impedance features (e.g., diffusion) that would otherwise generate diverging long-timescale DRT peaks. Nonetheless, some ambiguity in the DRT-DOP deconvolution is unavoidable because the distributions can interact, potentially leading to small DRT pseudo-peaks at long timescales. Consequently, the DRT-DOP framework is best regarded as a semi-quantitative tool for visualizing dominant processes and guiding the development of quantitative models, such as equivalent circuit models. Further details and a free Python package are available in previous studies.[18,22]

For the In | $Li_{5.5}PS_{4.5}Cl_{1.5}$ | In/LiIn cell, the indium working electrode was discharged at a constant current of 0.672 mA cm^{-2} to an areal capacity of 5.76 mA h cm^{-2} and then charged at the same current to an upper cutoff voltage of 0.2 V vs In/LiIn. The *Operando* hybrid measurement was performed using the same parameters as for the S–C–$Li_{5.5}PS_{4.5}Cl_{1.5}$ half-cell. Only the DRT model (without the DOP complement) was applied to transform the time- and frequency-domain data for this cell, as no constant-phase processes were observed in the low-frequency range.

Raman spectroscopy

Raman spectroscopy was carried out using a Bruker Senterra II Raman microscope equipped with a 532 nm laser. All samples were mounted on a customized holder with a quartz window to prevent air exposure. Raman spectra were collected in a wavenumber range of 50–1425 cm^{-1} with an integration time of 5 s at a laser power of 2.5 mW, unless otherwise stated. A 1200 grating, providing a resolution of 1.5 cm^{-1}, and a 20x objective lens were used.

Powder X-ray diffraction

XRD measurements were conducted using a STOE STADIP diffractometer with Mo $K\alpha_1$ radiation (λ = 0.70930 Å) in Debye–Scherrer geometry. Samples were sealed in glass capillaries (Hilgenberg, 0.5 mm diameter). The diffraction patterns were collected with a step size of 0.015°.

X-ray photoelectron spectroscopy

XPS measurements were carried out using a PHI GENESIS spectrometer. *Ex situ* samples were prepared following the same procedure used for XAS. The samples were mounted on a holder in an Ar-filled glove box and transferred to the instrument using an air-tight transfer shuttle. Monochromatic Al Kα radiation (1486.6 eV) was used with a power of 25 W and an accelerating voltage of 15 kV. The beam diameter was 100 µm, and the pass energy was set to 27 eV. To clean the surface, the samples were sputtered using an Ar^+ sputter gun with a raster size of 3 x 3 mm^2 at an energy of 0.5 kV for 30 s prior to measurements. The samples were neutralized using a charge neutralizer.

Data evaluation was performed using CasaXPS software. The binding energies were calibrated by taking the C 1s signal of adventitious carbon (284.8 eV) as the reference. Afterward, the S 2p and Se 3p spectra of the S–C–Li_6PSe_5Br cathodes were calibrated using the S 2p PS_4^{3-} component as an internal reference. Peak fitting was conducted using a Shirley background and GL(30) line shapes, constraining FWHM. The spin–orbit splittings for Se 3p and S 2p were set to 5.8 and 1.16 eV, respectively. The area ratio of S $2p_{1/2}$ to S $2p_{3/2}$ doublet was constrained to 1:2. The theoretical area ratio of 0.5 for the Se 3p doublet did not provide a satisfactory fit for the Li_2Se and elemental selenium reference spectra. Instead, an empirical area ratio of 0.41 has been reported in a previous study.[24] Therefore, the area ratio of the Se 3p doublet was first left unconstrained and evaluated, and the resulting values were 0.378 and 0.382 for Li_2Se and elemental selenium, respectively. Based on these values, the area ratio of Se $3p_{1/2}$ to Se $3p_{3/2}$ was fixed at 0.38 for all samples.

3. Results

3.1 Asymmetric Sulfur Redox Behavior with a Highly Conductive Sulfide SE

A solid-state Li–S cell employing $Li_{5.5}PS_{4.5}Cl_{1.5}$ as the catholyte is constructed and its redox mechanism is investigated using electrochemical and spectroscopic characterization methods. A S–C–$Li_{5.5}PS_{4.5}Cl_{1.5}$ composite cathode was prepared through an intensive ball-milling process to enable high sulfur utilization and allow investigation under realistic Li–S cell operating conditions. The voltage window was set to achieve a high specific capacity while minimizing contributions from SE decomposition. Argyrodite sulfide SE are known to undergo phosphorous reduction when cells are discharged below 0.6 V vs In/LiIn.[25,26] Therefore, the lower cut-off voltage of 1.0 V vs In/LiIn was employed, and the upper cut-off voltage of 2.4 V vs In/LiIn was used to enable reversible cycling. To assess the contribution of SE decomposition, a C–$Li_{5.5}PS_{4.5}Cl_{1.5}$ half-cell was cycled within this voltage window and exhibits a negligible initial discharge capacity (Figure S1a), indicating that SE decomposition is minimal during the initial discharge under these cycling conditions.

Figure 1a,b shows the voltage profile of the S–C–$Li_{5.5}PS_{4.5}Cl_{1.5}$ half-cell and corresponding dQ/dV plot in the voltage range of 1.0–2.4 V vs In/LiIn during the initial discharge and charge at 25 °C. The sulfur loading was 4.0 mg cm^{-2}, which is within the range of practical electrode loadings for solid-state Li–S batteries. The cell delivered a specific capacity of 1352 mA h g^{-1} during first discharge, corresponding to 81% of the theoretical capacity of sulfur (1675 mA h g^{-1}). Notably, the voltage profile exhibits asymmetry between discharge and charge, which is characterized by two voltage plateaus during discharge and a single plateau during charge. Since the C–$Li_{5.5}PS_{4.5}Cl_{1.5}$ cell delivered a negligible capacity during the initial discharge, the two observed voltage plateaus during discharge can be attributed to sulfur reduction reactions. This asymmetric redox behavior is further evidenced by the dQ/dV plot exhibiting two reduction peaks at 1.37 and 1.27 V and a single oxidation peak at 1.77 V, in which the single oxidation peak appears to consist of a small shoulder and large peak overlapping. Under slower kinetics at 0 °C, the oxidation peaks are more separated and become distinguishable, as shown in Figure S1b,c. These low-temperature data suggest that there may be at least two processes during charge, contrary to a previous suggestion,[9] although they cannot be readily distinguished using only galvanostatic charge–discharge tests.

To examine whether these two processes during charge could be resolved by overpotential relaxation or by enhanced reaction kinetics, galvanostatic intermittent titration technique (GITT) measurements and high-

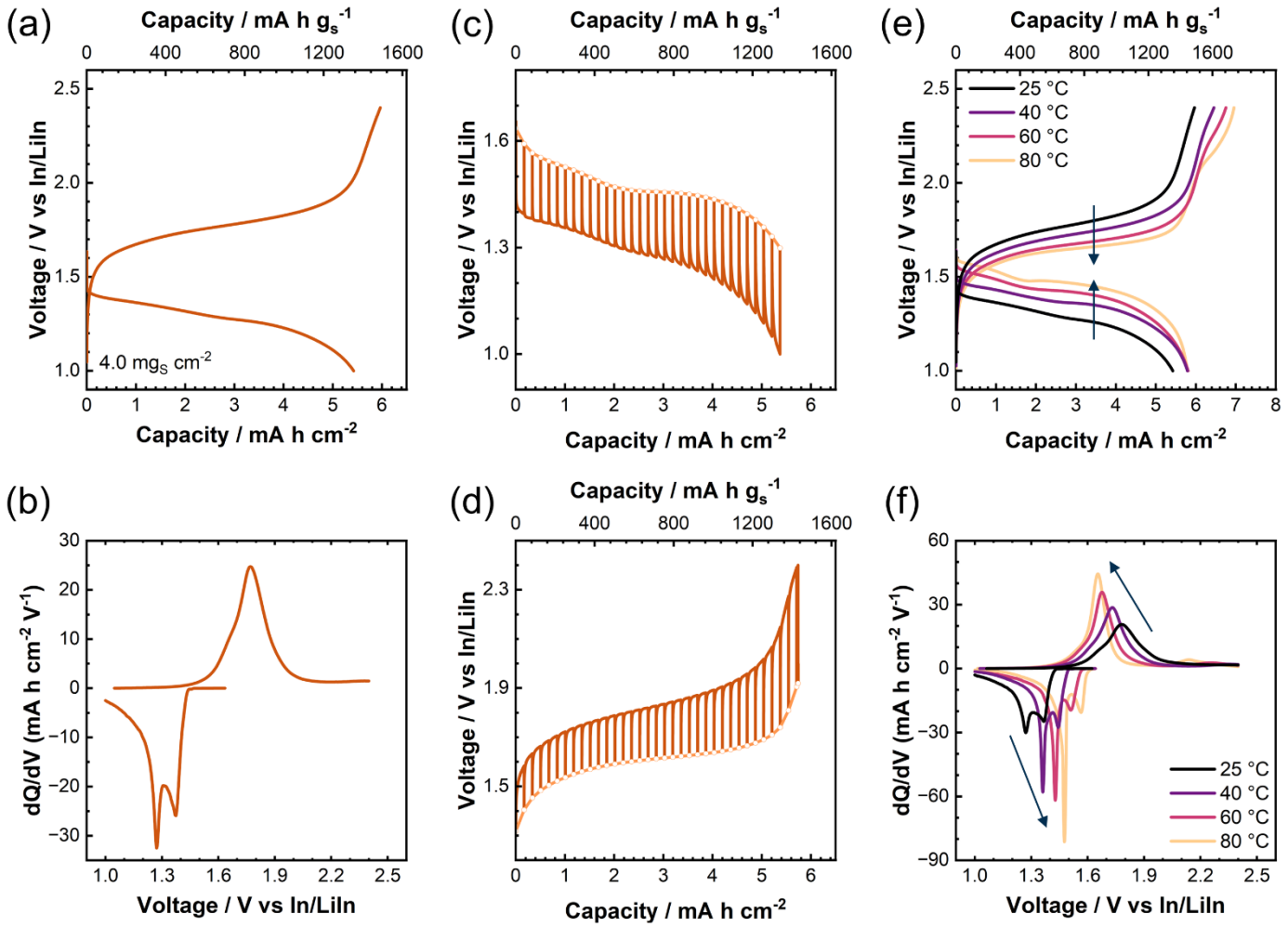

Figure 1: (a) Initial discharge–charge voltage profile and (b) corresponding d*Q*/d*V* plot of the S–C–$Li_{5.5}PS_{4.5}Cl_{1.5}$ half-cell at 0.1C and 25 °C. GITT curves during the initial (c) discharge and (d) charge, obtained with a pulse current of 0.1C for 15 min, followed by 10 h relaxation period at 25 °C. (e) Initial discharge–charge voltage profiles and (f) corresponding d*Q*/d*V* curves of the S–C–$Li_{5.5}PS_{4.5}Cl_{1.5}$ half-cells at 0.1C operated at 25, 40, 60, and 80 °C.

temperature discharge–charge tests were performed. **Figure 1**c,d shows QOCV curves obtained from GITT measurements at 25 °C. Although overpotentials of approximately 0.2 V are relaxed during both discharge and charge, the QOCV curves still exhibit two voltage plateaus during discharge and only a single plateau during charge. High temperature discharge–charge profiles at 40, 60, and 80 °C are shown in **Figure 1**e,f. Increasing temperature reduces polarization, as indicated by the smaller voltage gap between discharge and charge, while the asymmetric redox behavior observed at room temperature is maintained. These electrochemical results support the notion that the S–C–$Li_{5.5}PS_{4.5}Cl_{1.5}$ half-cell undergoes an intrinsically asymmetric reaction pathway rather than just having a large degree of polarization that could be mitigated by relaxation or enhanced kinetics at elevated temperatures.

To further elucidate this asymmetric reaction pathway and sulfur intermediate species in SSB, *ex situ* XAS was carried out on S–C–$Li_{5.5}PS_{4.5}Cl_{1.5}$ cathodes retrieved at various depth of discharge (DOD) and state of charge (SOC) levels. Reference S K-edge XAS spectra of elemental sulfur (S_8), Li_2S, and $Li_{5.5}PS_{4.5}Cl_{1.5}$ were collected to assign sulfur-containing species in the composite cathode (Figure S2a). Elemental sulfur exhibits a characteristic absorption feature at 2472 eV, corresponding to the transition from S 1s to S-S π* state.[27] Li_2S is characterized by two main absorption peaks at 2473 and 2475.5 eV, and the absorption edge of $Li_{5.5}PS_{4.5}Cl_{1.5}$ SE appears at 2471 eV. **Figure 2**a,b presents the *ex situ* S K-edge spectra of the S–C–$Li_{5.5}PS_{4.5}Cl_{1.5}$ cathode during the initial discharge and charge. The pristine cathode spectrum is dominated by

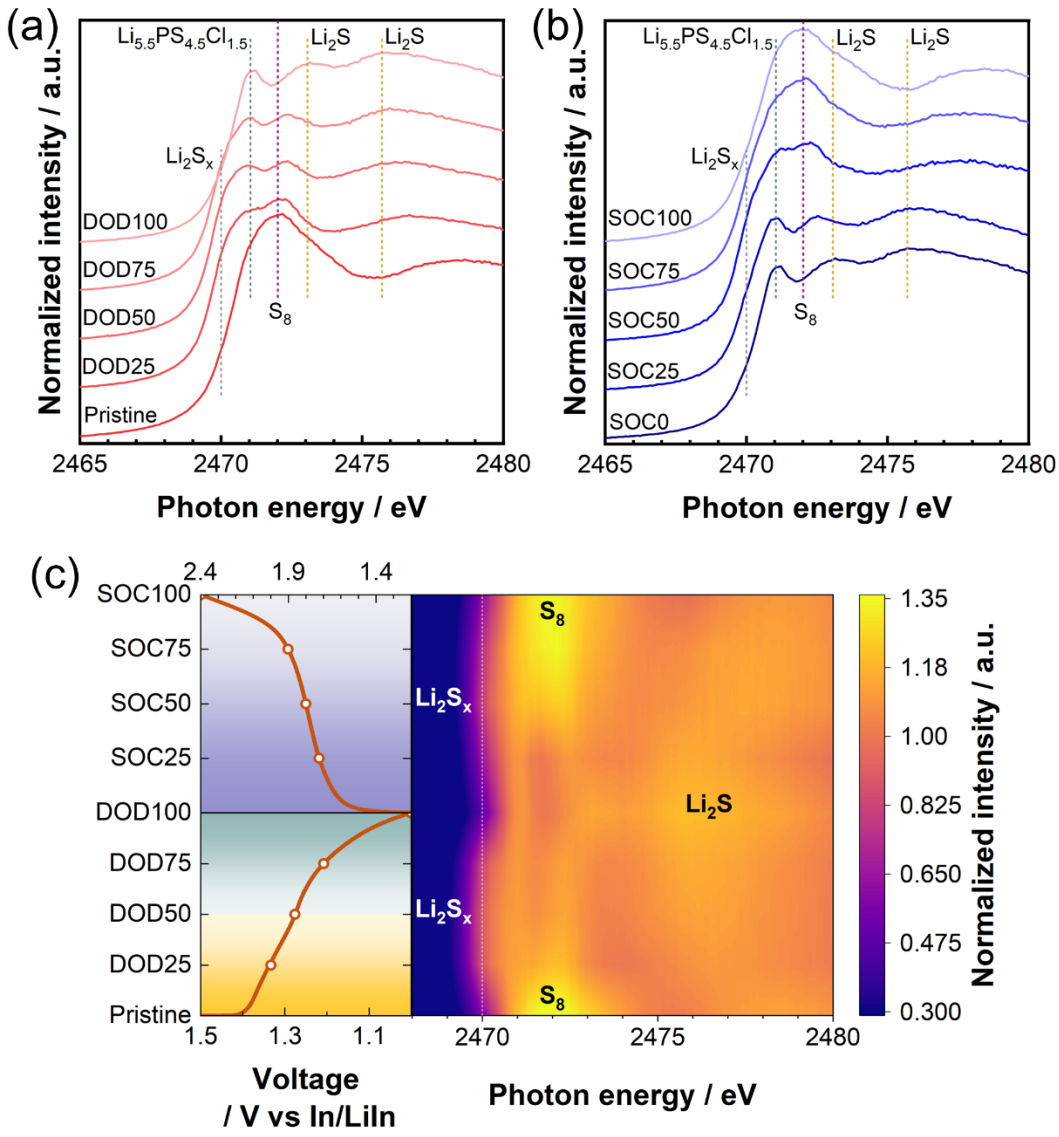

Figure 2: *Ex situ* S K-edge XAS spectra of S–C–$Li_{5.5}PS_{4.5}Cl_{1.5}$ cathodes recovered at various DOD and SOC states during the initial (a) discharge and (b) charge. The spectrum at SOC0 in (b) corresponds to the fully discharged state (DOD100) shown in (a). (c) Contour map showing the evolution of the *ex situ* S K-edge XAS spectra during the initial discharge and charge.

the absorption feature of elemental sulfur at 2472 eV. Upon discharge to DOD50, the contribution from elemental sulfur decreases, accompanied by the emergence of a pre-edge peak at 2470 eV, which is attributed to reduced terminal sulfur in lithium polysulfide (Li_2S_x) species.[28] The pre-edge feature is clearly observable in the overlaid XAS spectra in Figure S2b,c. Additionally, the absorption feature of the $Li_{5.5}PS_{4.5}Cl_{1.5}$ SE, whose absorption edge partially overlaps with elemental sulfur, becomes more distinguishable as the sulfur contribution decreases. With further discharge, the pre-edge peak of Li_2S_x disappears and the characteristic features of Li_2S at 2473 and 2475.5 eV grow in intensity. At the fully discharged state (DOD100), the spectrum is dominated by contributions from Li_2S and $Li_{5.5}PS_{4.5}Cl_{1.5}$, indicating high sulfur utilization, consistent with the high discharge capacity observed by electrochemical characterization. In the early stage of charge, from SOC0 to SOC25, Li_2S is partially converted to Li_2S_x. Unlike discharge, further charging from SOC25 to SOC50 leads to the simultaneous formation of Li_2S_x and elemental sulfur. Notably, elemental sulfur begins to reappear at low SOC levels before Li_2S is fully oxidized to Li_2S_x. Upon continued charging, the absorption peaks of Li_2S and Li_2S_x diminish, accompanied by the growth of the elemental sulfur feature. At SOC100, the spectrum becomes similar to that of the pristine cathode.

The distinct evolution of sulfur species during discharge and charge is shown in the contour plot of *ex situ* XAS spectra (**Figure 2**c). During discharge, elemental sulfur undergoes a two-step conversion to Li_2S via Li_2S_x intermediates, whereas charging proceeds through overlapping reactions rather than discrete steps. This result further clarifies that, although the asymmetric sulfur reaction pathway is evident in the galvanostatic charge–discharge profiles, the seemingly single reaction during charge consists of two largely overlapping reactions corresponding to the two distinct reduction steps observed during discharge.

Since all lithium polysulfide species (Li_2S_x, x = 2–8) exhibit a pre-edge feature at 2470 eV, S K-edge XAS alone is insufficient to distinguish specific lithium polysulfide species.[29] Therefore, Raman spectroscopy was employed as a complementary method to further identify sulfur species in the composite cathode (Figure S3). The pristine S–C–$Li_{5.5}PS_{4.5}Cl_{1.5}$ cathode exhibits weak vibrational features of elemental sulfur, while no characteristic Raman modes of $Li_{5.5}PS_{4.5}Cl_{1.5}$ are detected. Notably, no features of elemental sulfur are observed for the C–$Li_{5.5}PS_{4.5}Cl_{1.5}$ (mass ratio C:SE = 1:9) sample at low laser power, whereas characteristic sulfur peaks appear at high laser power despite the absence of sulfur in the composite. These observations may be attributed to strong light absorption by the carbon black additive and the resulting local thermal decomposition, indicating that Raman spectroscopy may introduce measurement artifacts in carbon-

containing composites. Because of these spectral artifacts, it was difficult to identify the lithium polysulfide species in the cathode after discharge/charge.

Electrochemical impedance spectroscopy (EIS) is an effective technique for characterizing electrochemical processes in battery systems. To investigate the evolution of impedance during cycling of solid-state Li–S batteries, *operando* frequency- and time-domain (hybrid) impedance spectroscopy was performed. EIS is typically carried out in frequency-domain, which provides high accuracy but requires long acquisition times, particularly in the low frequency range. In contrast, time-domain approaches offer rapid measurement time but are limited by poor accuracy at high frequencies. By applying two techniques in different frequency ranges, the hybrid measurement combines the strengths of both methods while mitigating measurement noise with DRT-assisted data transformation, enabling rapid and reliable EIS over a broad frequency range.[18,22] **Figure 3**a shows the time-domain measurement with step current excitation and the conventional galvanostatic EIS (GEIS) in the frequency-domain, both implemented *operando* during constant-current charge and discharge.

The acquired data were analyzed using a combined DRT and DOP model.[18,22] The DRT represents the impedance as an infinite series of parallel resistor-capacitor (RC) elements, corresponding to relaxation processes $\gamma(\ln \tau)$ distributed over log-timescales $\ln \tau$. The relationship between the impedance and DRT is given by equation (1).

$$Z_\gamma(\omega) = \int_{-\infty}^{\infty} \frac{\gamma(\ln \tau)}{1 + j\omega\tau} d\ \ln \tau \qquad (1)$$

However, when the system includes non-RC type responses, such as Warburg diffusion or capacitance, the DRT may fit the data poorly and/or provide misleading interpretations due to the appearance of multiple peaks for a single process. Therefore, the DOP has been introduced as a complementary model by a previous study.[18,22] DOP describes the impedance as an infinite series of constant phase elements (CPE), representing phasances $\rho(v)$ over their orders v, which can be converted into phase angles $\theta = v\pi/2$. The CPE-type impedance is correlated to the phasances according to equation (2).

$$Z_\rho(\omega) = \int_{-1}^{1} \rho(v)(j\omega)^v\ d\ v \qquad (2)$$

The combined DRT-DOP model allows the separation of impedance into RC- and CPE-type contributions as expressed in equation (3), where R_0 represents the ohmic resistance.

$$Z = R_0 + Z_\gamma(\omega) + Z_\rho(\omega) \qquad (3)$$

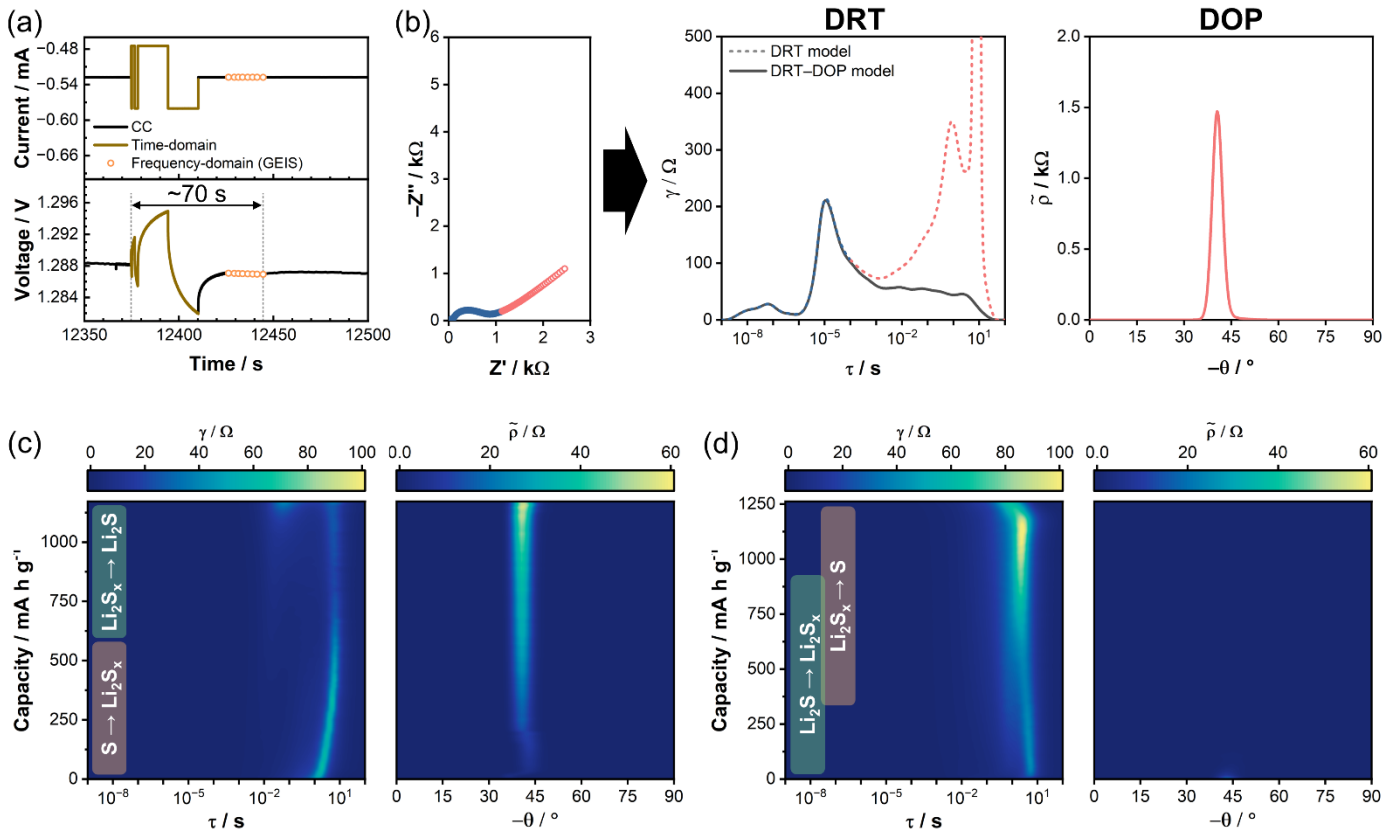

Figure 3: (a) *Operando* impedance spectroscopy using time- and frequency-domain measurements with accelerated acquisition time. (b) Schematic illustration of the DRT-DOP model, demonstrating the separation of constant-phase processes from the conventional DRT model. 2D DRT-DOP mapping of the S–C–$Li_{5.5}PS_{4.5}Cl_{1.5}$ half-cell during the initial (c) discharge and (d) charge, with the corresponding conversion reactions characterized by *ex situ* S K-edge XAS represented in the insets. In both (c) and (d), the left and right panels represent the 2D DRT and DOP plots, respectively.

The separation of RC- and CPE-type processes is illustrated using an exemplary Nyquist plot (**Figure 3**b). Both the conventional DRT and the DRT-DOP transforms were applied to the impedance data corresponding to the Nyquist plot showing a semicircle followed by a diffusion tail, which can be approximately interpreted using an electrochemical equivalent circuit model consisting of R//CPE and CPE elements in series. Multiple overlapping relaxation processes distributed over a broad frequency range are observed in the conventional DRT transform. In contrast, the DRT-DOP model shows a significant relaxation process at $\tau \sim 10^{-5}$ s in the DRT plot, which is attributed to the semi-circle in the Nyquist plot, while a peak at $-\theta \approx 42°$ in the DOP plot corresponds to the diffusion tail. The interpretation based on the DRT-DOP model is consistent with the conventional understanding of the system derived from electrochemical equivalent circuit model, demonstrating the utility of the DRT-DOP transformation for interpretable impedance analysis.

The DRT-DOP model was applied to the *operando* impedance data of S–C–$Li_{5.5}PS_{4.5}Cl_{1.5}$ half-cell during the initial discharge and charge at 0.1C and 25 °C. To evaluate the contribution from the In/LiIn anode, the two-dimensional (2D) DRT plots of the In | $Li_{5.5}PS_{4.5}Cl_{1.5}$ | In/LiIn cell are analyzed (Figure S4). The relaxation processes from the In/LiIn anode shows γ values below 10 Ω, indicating insignificant contributions to the total impedance of the S–C–$Li_{5.5}PS_{4.5}Cl_{1.5}$ half-cell. Nevertheless, at the end of charge, a resistive relaxation process is observed at $\tau \sim 10^{-1}$ s, which can be attributed to the dealloying process and the depletion of Li in the In/LiIn anode.[30] **Figure 3**c,d shows the evolution of resistance in the S–C–$Li_{5.5}PS_{4.5}Cl_{1.5}$ half-cell represented in the 2D DRT and DOP plots. During discharge, a dominant process is observed in the 2D DRT plot, which shifts to longer timescales while maintaining a nearly constant resistance until the middle of discharge. The detailed one-dimensional (1D) DRT and DOP plots extracted from the 2D mapping for 20% DOD and SOC intervals are shown in Figure S5. The 1D DRT plots at 0, 20, and 40% DOD exhibit a dominant relaxation at $\tau \sim 1$–10 s and less pronounced processes at shorter timescales. While it is difficult to unambiguously resolve overlapping electrochemical processes, we interpreted the underlying processes based on their characteristic timescales. Typically, in the timescale range of 10^{-2}–10 s, the observed processes include charge transport through the solid-electrolyte interface and charge transfer at the cathode and anode, as well as diffusion.[31,32] As CPE-type contributions are separately assessed in the DOP model, the impedance features in the DRT plot are mainly derived from RC-type processes other than diffusion. Furthermore, as previously discussed and supported by Figure S4, the impedance contribution of the In/LiIn anode is insignificant relative to the overall cell impedance. Therefore, the processes at long timescales $\tau \sim 10^{-2}$–10 s can be reasonably attributed to the impedance of the cathode–electrolyte interface (CEI) and the charge transfer at the cathode active material.[32–34] The process at $\tau \sim 10$ s becomes less resistive after the middle of discharge. Based on the two-step sulfur conversion during discharge identified by XAS, the conversion from sulfur to Li_2S_x corresponds to a highly resistive process during the first reduction step due to the electronically and ionically insulating character of S_8 (conductivity of ~10^{-30} S cm^{-1}).[4] In contrast, the reaction product of the subsequent conversion, Li_2S, is still poorly conducting but exhibits a conductivity several orders of magnitude higher (conductivity of 10^{-14} – 10^{-10} S cm^{-1})[35–37] than S_8, thereby mitigating the CEI impedance and/or the charge transfer resistance at the cathode active material. At the end of discharge, a substantial resistive process emerges at $\tau \sim 10^{-1}$ s, which is attributed to relaxation processes from the In/LiIn anode, as previously detected in the In | $Li_{5.5}PS_{4.5}Cl_{1.5}$ | In/LiIn cell presented in Figure S4. Throughout

discharge, a single process is consistently observed in the 2D DOP plot at $-\theta \approx 42°$, which is close to the 45° phase angle of a Warburg element and can likely be attributed to Li^+ diffusion process at the cathode.[22]

During charge, two major processes are observed in the 2D DRT plot. One process at $\tau \sim 10$ s appears from the beginning of charge, and an additional process emerges at $\tau \sim 1$ s. These processes also can be attributed to the CEI impedance and/or the charge transfer resistance at the cathode active material. Upon continued charging, two resistive processes merge into one and exhibit increased resistance. Based on the XAS results, the increased resistance observed in the DRT plot can be correlated with the formation of insulating sulfur. Meanwhile, the lack of significant DOP peaks indicates that there is insignificant diffusion contribution to impedance.

The conventional DRT model was not well suited for analyzing the *operando* hybrid impedance data of solid-state Li–S batteries, as indicated by the 2D DRT plots obtained without the DOP model (Figure S6). The overall resistances of the relaxation processes are comparable during discharge and charge, which is clearly inconsistent with the DRT-DOP results. The origin of this misleading interpretation can be understood from comparison with the Nyquist spectra calculated from the DRT-DOP plots over the frequency range from 1 MHz to 10 mHz (Figure S7). During discharge, a low frequency tail gradually appears in addition to the semicircular response, whereas during charge the spectra maintain a semicircular shape. Because the conventional DRT model artificially transforms these diffusion processes during discharge into relaxation processes, the relaxation process resistance in the conventional DRT plot is overestimated. This discrepancy between the DRT-DOP and conventional DRT models indicates that the DRT-DOP model is more suitable for electrochemical systems involving diffusion processes.

Since sulfur is ionically and electronically insulating, sulfur conversion reactions can occur only at the triple-phase boundaries between sulfur, SE, and carbon additives. This concept has been utilized to improve the electrochemical performance of solid-state Li–S batteries, for instance, by employing mixed ionic–electronic conductors or surficial redox mediators.[38–40] In addition to improving performance, further insight into the reaction mechanism in solid-state Li–S batteries can be proposed by correlating these triple-phase boundary constraints with the impedance data and the intermediate reaction products. The limitation in reaction sites suggests that the conversion products likely nucleate and grow from the triple-phase boundaries. XAS results reveal that Li_2S_x and Li_2S are formed stepwise during discharge, whereas the formation of Li_2S_x and sulfur overlaps during charge. In both cases, the sulfur conversion products are expected to progressively passivate

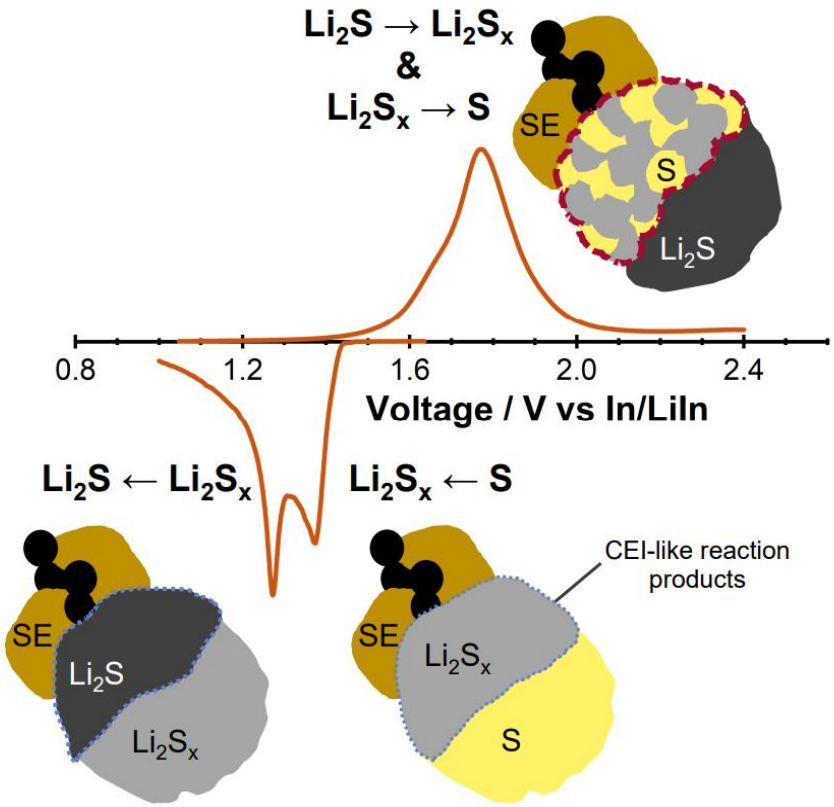

Figure 4: Schematic illustration of conversion reaction products propagating from the triple-phase boundary. This conceptual CEI-like passivation model is proposed by correlating the triple-phase boundary constraints with asymmetric sulfur conversion pathways and impedance evolution, observed in ex situ XAS and operando impedance spectroscopy results. Each conversion reaction step is represented on the corresponding d*Q*/d*V* peak.

the unreacted active material at the triple-phase boundary, as conceptually illustrated in **Figure 4**. These reaction products exhibit different resistive behaviors during discharge and charge depending on their transport properties, which are reflected in the impedance evolution characterized by *operando* impedance spectroscopy combined with the DRT-DOP model. Notably, the charge transport through the CEI and/or charge transfer at the cathode exhibit higher resistance during charge than during discharge. This observation can be attributed to the formation of insulating sulfur at low SOCs during charging, which impedes the conversion reactions more severely than the discharge products, Li_2S and Li_2S_x. These behaviors support the proposed model where the accumulated products between the unreacted active material and the triple-phase boundary act as a CEI-like layer.

3.2 Se – S Exchange Reaction-Driven Formation of Li–Se SSB

When sulfur is present in the SE of solid-state Li–S batteries, the identification of intermediate species becomes challenging. For sulfur-specific spectroscopic methods such as XPS and XAS, the spectra contain sulfur signals from the SE in addition to those from the active material sulfur. Moreover, since SE are prone to decompose within the operating voltage range of typical Li–S cells, their decomposition products may share common intermediate species with sulfur redox products. Therefore, if sulfur-free SE exhibit sufficiently high ionic conductivity and compatibility with sulfur, they possess the potential to facilitate sulfur-specific spectroscopic investigation without the spectral overlap between the SE and the active material sulfur. Furthermore, they provide the opportunity to estimate the respective capacity contributions from SE decomposition and active material redox.

Therefore, another sulfur composite cathode was prepared using Li_6PSe_5Br, which contains selenium substituting for sulfur in argyrodite sulfide SE and exhibits a high ionic conductivity of 5 mS cm^{-1}.[41] The composite cathode was prepared with the same procedure used for the S–C–$Li_{5.5}PS_{4.5}Cl_{1.5}$, except that the amount of Li_6PSe_5Br was increased to account for its higher mass density compared to $Li_{5.5}PS_{4.5}Cl_{1.5}$, ensuring comparable volumetric phase fractions. **Figure 5**a,b shows the voltage profile of the S–C–Li_6PSe_5Br half-cell and corresponding dQ/dV plot in the voltage range of 1.0–2.4 V vs In/LiIn during the initial discharge and charge at 25 °C. The S–C–Li_6PSe_5Br half-cell delivered an areal capacity of 5.23 mA h cm^{-2}, corresponding 78% of the calculated theoretical capacity. The dQ/dV plot exhibits a small shoulder reduction peak at 1.40 V and a large reduction peak at 1.33 V during discharge. Upon subsequent charging, a single oxidation peak appears at 1.68 V, which is approximately 0.1 V lower than that observed for the S–C–$Li_{5.5}PS_{4.5}Cl_{1.5}$ half-cell, suggesting a different redox mechanism. Nevertheless, the asymmetric feature, characterized by two reduction peaks and a single oxidation peak, is similar to that of the S–C–$Li_{5.5}PS_{4.5}Cl_{1.5}$ half-cell. To examine the equilibrium potential under reduced polarization, QOCV curves were obtained using GITT (**Figure 5**c, d). The QOCV curves differ from the galvanostatic discharge–charge profiles. While the discharge QOCV curve consistently exhibits two voltage plateaus at 1.46 and 1.41 V, the charge QOCV curve shows two distinct plateaus at 1.52 and 1.62 V, representing one additional plateau compared to that observed in the galvanostatic discharge–charge profiles. This difference is more clearly presented by comparing the galvanostatic discharge–charge profiles with the QOCV curves extracted from GITT profiles (Figure S8). These results indicate that the redox mechanism of the S–C–Li_6PSe_5Br half-cell is distinct from that of the S–C–$Li_{5.5}PS_{4.5}Cl_{1.5}$ half-cell.

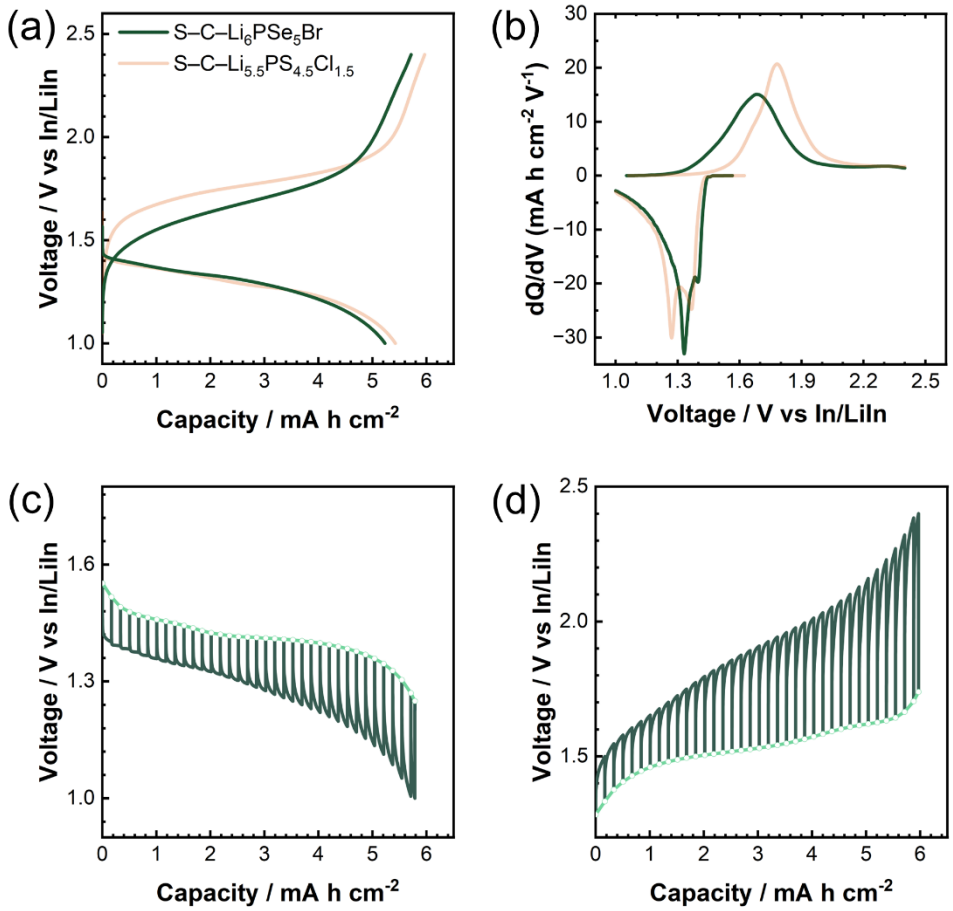

Figure 5: (a) Initial discharge–charge voltage profile and (b) corresponding d*Q*/d*V* plot of a half-cell incorporating the S–C–Li_6PSe_5Br cathode at 0.1C and 25 °C. For comparison, the corresponding data for the S–C–$Li_{5.5}PS_{4.5}Cl_{1.5}$ half-cell are included in (a) and (b). GITT curves during the initial (c) discharge and (d) charge, obtained with a pulse current of 0.1C for 15 min, followed by 10 h relaxation period at 25 °C.

To investigate the origin of the distinct chemistry in the S–C–Li_6PSe_5Br cathode composite, XAS, Raman spectroscopy, XRD, and XPS analyses were performed. **Figure 6**a presents the S K-edge XAS spectrum of the pristine S–C–Li_6PSe_5Br cathode together with reference spectra. The spectrum of the pristine cathode closely matches the $Li_{5.5}PS_{4.5}Cl_{1.5}$ SE rather than elemental sulfur, in contrast to the pristine S–C–$Li_{5.5}PS_{4.5}Cl_{1.5}$ spectrum, which is dominated by the elemental sulfur feature. This indicates that most of sulfur exists in reduced sulfur species, such as PS_4^{3-} and S^{2-}, with an oxidation state of −II, rather than in form of elemental sulfur S(0). To gain further insight into the sulfur chemical states, Raman spectroscopy was conducted on the S–Li_6PSe_5Br composite instead of the S–C–Li_6PSe_5Br cathode composite due to the above-mentioned difficulty in acquiring reliable Raman spectra from carbon-containing samples (**Figure 6**b). The S–Li_6PSe_5Br composite was prepared through the same ball-milling process used for the S–C–Li_6PSe_5Br

cathode, except that carbon black was excluded. Li_6PSe_5Br SE exhibits a symmetric stretching mode of the PSe_4^{3-} unit at 236 cm^{-1}.[41,42] However, the ball-milled S–Li_6PSe_5Br composite shows a broad peak at 256 cm^{-1}, implying a substantial structural change in Li_6PSe_5Br during the ball-milling process with elemental sulfur. This broad peak is a main feature of ball-milled selenium, as shown in Figure S9, indicating that amorphous selenium was formed.[43] Furthermore, a peak located at 418 cm^{-1} matches the symmetric stretching mode of the PS_4^{3-} tetrahedra in the Li_6PS_5Br sulfide SE.[44] The disappearance of the PSe_4^{3-} unit, along with the emergence of the PS_4^{3-} unit and amorphous selenium, suggests substitution of selenium by sulfur within the PSe_4^{3-} unit during the ball-milling process, leading to the formation of PS_4^{3-} tetrahedra and amorphous selenium.

We examined this structural change using XRD. **Figure 6**c shows the XRD pattern of the ball-milled S–Li_6PSe_5Br composite. The diffraction peaks are significantly broadened due to the harsh ball-milling conditions. However, characteristic reflections corresponding to the argyrodite structure are still observed. Notably, the peak positions are identical to those of Li_6PS_5Br, implying that most of selenium in Li_6PSe_5Br, including free Se^{2-} and selenium in PSe_4^{3-} units, was substituted by sulfur during ball milling, which is consistent with the XAS and Raman results. Additionally, to increase the crystallinity of the SE and compare its diffractogram with the reference material, the ball-milled S–Li_6PSe_5Br composite was annealed in a carbon-coated ampoule at 300 and 400 °C for 5 h under vacuum (Figure S10). After annealing, the reflections

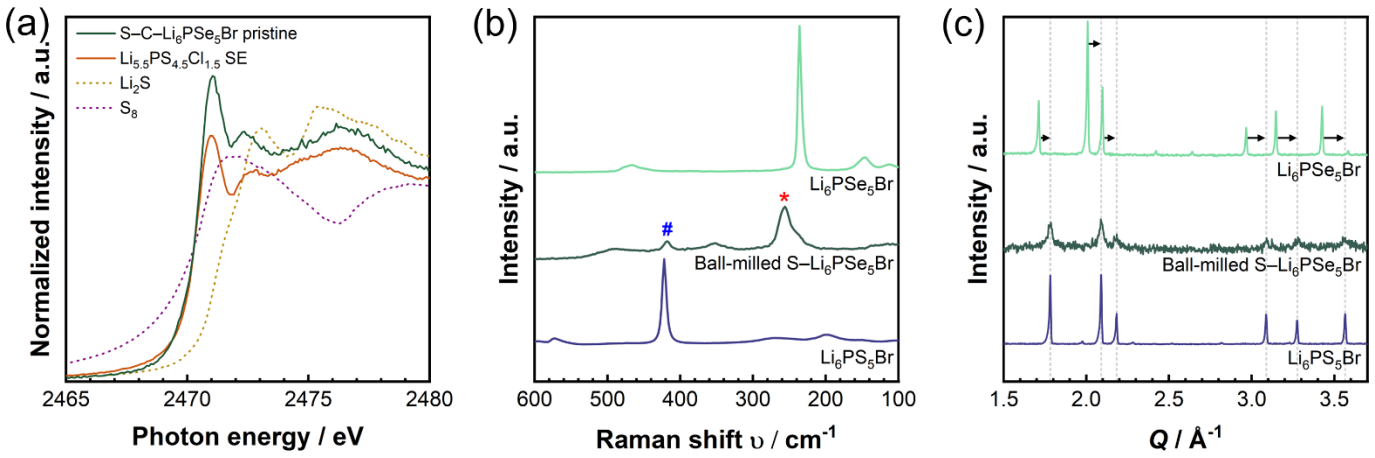

Figure 6: (a) S K-edge XAS spectrum of the pristine S–C–Li_6PSe_5Br cathode along with reference spectra of $Li_{5.5}PS_{4.5}Cl_{1.5}$, Li_2S, and elemental sulfur. (b) Raman spectrum and (c) XRD pattern of the ball-milled S–Li_6PSe_5Br composite along with reference Raman spectra and diffraction patterns of Li_6PSe_5Br and Li_6PS_5Br, respectively.

exhibited increased intensities while maintaining their positions, supporting that most of selenium was replaced by sulfur during the ball-milling process.

Taken together, these observations suggest that sulfur is thermodynamically more stable than selenium in the argyrodite structure. Because sulfur has a higher electronegativity (2.58) and a smaller ionic radius for S^{2-} (1.84 Å) than selenium (EN = 2.55 and r(Se^{2-}) = 1.98 Å),[45,46] the P–S covalent bond and the Coulombic interaction between Li^+ and S^{2-} are expected to be stronger than their selenium counterparts. Furthermore, formation energies obtained from the Open Quantum Materials Database (OQMD) and the Materials Project support the higher stability of sulfur in SE structures. For instance, the formation energy of Li_3PS_4 (−1.112 eV/atom, *Pnma*, OQMD-687436) is lower than Li_3PSe_4 (−0.810 eV/atom, *Pnma*, OQMD-1345149),[47,48] and the formation energy of Li_7PS_6 (−1.287 eV/atom, *Pna2₁*, mp-1211324) is also lower than Li_7PSe_6 (−1.118 eV/atom, *Pna2₁*, mp-1211446).[49] Therefore, the energy generated during ball milling induces an Se – S exchange reaction between elemental sulfur and selenide SE due to the higher thermodynamic stability of sulfide SE.

To evaluate whether the atomic percentage of sulfur in the S–C–Li_6PSe_5Br composite was sufficient to fully replace selenium in Li_6PSe_5Br, the elemental composition of the S–C–Li_6PSe_5Br composite was calculated, as summarized in Table S1. The atomic percentage of sulfur (23.2%) is higher than that of selenium (19.4%), indicating that a sufficient amount of sulfur is present to enable the near-complete Se – S exchange reaction. Moreover, because the sulfur amount exceeds that of selenium, excess elemental sulfur (corresponding to 16.2 at% of the total sulfur in the composite cathode) remains unincorporated into the Li_6PS_5Br structure and can contribute to redox reactions as an active material during discharge and charge. The resulting composition of the electrochemically active chalcogen species is 83.8 at% selenium and 16.2 at% sulfur, based on complete Se – S exchange. Due to the complex Se – S exchange reaction as well as the presence of residual sulfur, it is impossible to accurately determine the mass of electrochemically active materials in the S–C–Li_6PSe_5Br composite. Therefore, the specific capacity of the S–C–Li_6PSe_5Br half-cell cannot be determined. Instead, the areal capacity was used, because the total molar amount of chalcogen species in the cathode remains constant despite the Se – S exchange reaction.

The residual sulfur redox behavior was examined by *ex situ* S K-edge XAS during initial discharge and charge (**Figure 7**a,b). The pristine cathode spectrum has dominant $Li_{5.5}PS_{4.5}Cl_{1.5}$-like features, which are attributed to Li_6PS_5Br formed by the Se – S exchange reaction, as previously observed by XRD. Because the amount

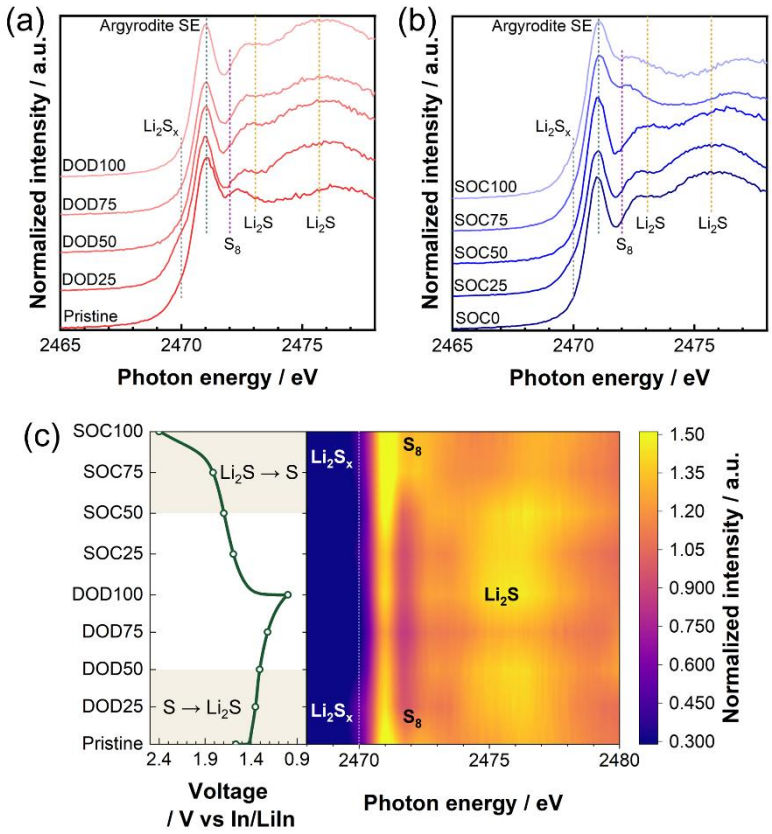

Figure 7: *Ex situ* S K-edge XAS spectra of S–C–Li_6PSe_5Br cathodes recovered at various DOD and SOC states during initial (a) discharge and (b) charge. The spectrum at SOC0 in (b) corresponds to the fully discharged state (DOD100) shown in (a). (c) Contour map showing the evolution of the *ex situ* S K-edge XAS spectra during the initial discharge and charge.

of residual sulfur is smaller compared to that of sulfur incorporated in the SE, its contribution to the spectrum is difficult to distinguish in the pristine state. During discharge, sulfur is converted into Li_2S via Li_2S_x intermediates. This conversion reaction is evidenced by the decreased intensity at 2472 eV and the appearance of the pre-edge peak of Li_2S_x at DOD25, along with the increased features of Li_2S at DOD50. The changes in the spectra are significant from DOD0 to DOD50, whereas the subsequent discharge and charge lead to minor spectral changes until SOC50. From SOC50 to SOC100, Li_2S is converted back into sulfur.

The overall sulfur redox behavior is shown in the contour plot of *ex situ* S K-edge XAS spectra (**Figure 7**c). The spectral changes corresponding to the conversion reaction between S_8 and Li_2S are most pronounced at the beginning of discharge and the end of charge, both of which lie in the high potential range. Moreover, the QOCV curves of the S–C–$Li_{5.5}PS_{4.5}Cl_{1.5}$ half-cell exhibit higher potentials than the Se–C–$Li_{5.5}PS_{4.5}Cl_{1.5}$ half-cell during both discharge and charge, demonstrating the higher potential of sulfur conversion reaction

compared to that of selenium (Figure S11). These results further account for the two distinct redox couples observed in the QOCV curves of the S–C–Li_6PSe_5Br half-cell (Figure 5c,d), which correspond to sulfur redox at higher potentials and selenium redox at lower potentials. The relative capacity ratio at each voltage plateau is close to the relative amount of each active material (atomic ratio Se:S = 83.8:16.2) calculated based on a near-complete Se – S exchange. These redox reactions of sulfur and selenium become distinguishable in the voltage profiles under high-temperature discharge–charge conditions (Figure S12).

The redox activity of chemically formed selenium was investigated by *ex situ* XPS at the pristine, fully discharged, and fully charged states over the binding energy range of 154–170 eV, which includes both the S 2p and Se 3p regions (Figure S13). For the pristine S–C–Li_6PSe_5Br cathode, S 2p signals show a main component at 161.6 eV attributed to the PS_4^{3-} unit[50,51] formed via the Se – S exchange reaction. Another S 2p peak at 163.2 eV can be assigned to bridging sulfur atoms in polysulfides[52,53] or S–S species in Se_xS_{8-x}.[54] A peak located at 161.1 eV corresponds to the Se $3p_{3/2}$ component of Se^0, accompanied by the corresponding Se $3p_{1/2}$ peak at 166.9 eV, with a spin–orbit splitting of 5.8 eV. At the fully discharged state, the Se^0 peak disappears, accompanied by the emergence of a signal at 159.2 eV assigned to Li_2Se. Residual S^0 also participates in the reduction reaction, as evidenced by the peak at 160.3 eV assigned to Li_2S.[53] Upon subsequent charging, the spectrum returns to that of the pristine cathode, with the reappearance of Se^0 and sulfur (–S^0–) signals. During discharging and charging, the PS_4^{3-} signal is consistently observed, implying that the SE formed via the exchange reaction is electrochemically stable within the applied voltage window. These observations reveal that selenium formed by the Se – S exchange reaction significantly contributes the delivered capacity.

The evolution of electrochemical processes in the S–C–Li_6PSe_5Br half-cell was examined at 0.1 C and 25 °C using *operando* hybrid impedance spectroscopy combined with the DRT-DOP transformation (**Figure 8**a,b). The detailed 1D DRT and DOP plots extracted from the 2D mapping for 20% DOD and SOC intervals are shown in Figure S14. At the beginning of discharge, a significant relaxation process appears in the 2D DRT plot at $\tau \sim 1$ s and shifts to longer timescales as discharge proceeds. With continued discharge, the γ value of this process varies while its timescale remains nearly constant. Additional less resistive processes are observed in the timescale range of 10^{-3} – 1 s, and the pronounced resistive process at the end of discharge appears at $\tau \sim 10^{-1}$ s, which can be attributed to the In/LiIn dealloying process.[30] The overall resistance in the DRT plot during discharge is much lower than that of the S–C–$Li_{5.5}PS_{4.5}Cl_{1.5}$ half-cell, with γ values below 30 Ω. This is because the conversion product Li_2Se is more electronically and ionically conductive than Li_2S

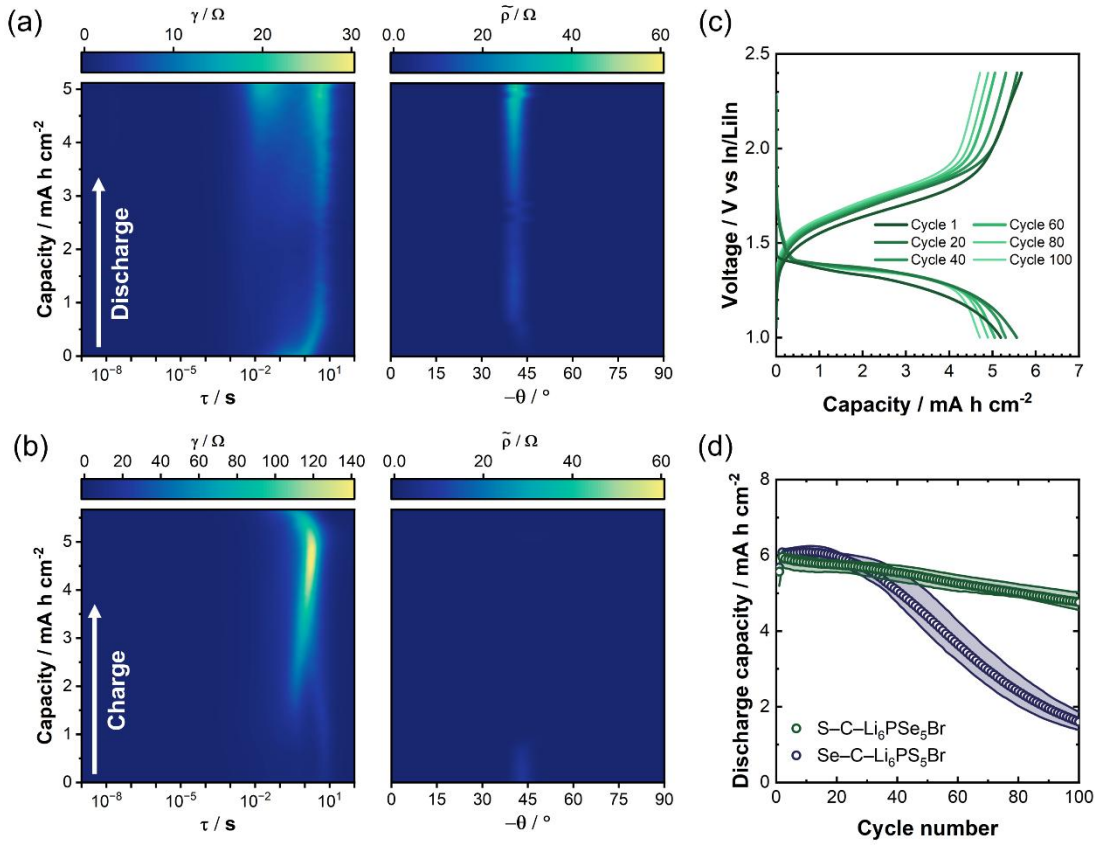

Figure 8: 2D DRT-DOP mapping of the S–C–Li_6PSe_5Br half-cell during the initial (a) discharge and (b) charge. In both (a) and (b), the left and right panels represent the 2D DRT and DOP plots, respectively. (c) Voltage profiles and (d) corresponding cycling performance of S–C–Li_6PSe_5Br half-cells at 0.1C and 25 °C. For comparison, the cycling performance of Se–C–Li_6PS_5Br half-cells is shown in (d). Data points and error bars in (d) represent the average and maximum/minimum values, respectively.

owing to its smaller band gap and lower Li^+ migration energy.[55–58] The higher conductivity of Li_2Se facilitates the charge transport through the CEI-like layer and/or the charge transfer at the cathode active material. Throughout discharge, the 2D DOP plot shows a single process that can be assigned to Li^+ diffusion process at the cathode, similar to that observed for the S–C–$Li_{5.5}PS_{4.5}Cl_{1.5}$ half-cell. During charge, the 2D DRT plot shows a process at $\tau \sim 10$ s in the early stage of charge, and an additional process appears at $\tau \sim 1$ s. As charge proceeds, these two processes merge into one that becomes highly resistive. This resistive process is likely attributed to the charge transport through the CEI and/or the charge transfer at the cathode active material, impeded by the conversion product selenium, which is more electronically conductive than sulfur[4,59] but likely lacks appreciable ionic conductivity due to the absence of Li^+ ions. The higher resistance of the relaxation processes during charge than during discharge in the S–C–Li_6PSe_5Br half-cell indicates, as in the S–C–$Li_{5.5}PS_{4.5}Cl_{1.5}$ half-cell, that the discharge and charge products of the selenium conversion reaction influence the cell impedance differently.

For comparison, a Se–C–Li_6PS_5Br half-cell was assembled using elemental selenium, Li_6PS_5Br sulfide SE, and carbon black, and its impedance evolution was examined. The composition of the Se–C–Li_6PS_5Br cathode was determined by excluding excess sulfur in the S–C–Li_6PSe_5Br cathode and directly employing elemental selenium and Li_6PS_5Br. The Se–C–Li_6PS_5Br half-cell also exhibits impedance evolution similar to that of the S–C–Li_6PSe_5Br half-cell, although the resistance of the electrochemical processes is slightly lower at the beginning of discharge and at the end of charge (Figure S15). The higher resistance of the S–C–Li_6PSe_5Br half-cell in these regions is attributed to the more resistive sulfur conversion reaction arising from residual sulfur after the Se – S exchange reaction during ball milling, as identified by *ex situ* S K-edge XAS (Figure 7c).

Figure 8c,d presents the discharge–charge profiles and corresponding cycling performance of the S–C–Li_6PSe_5Br half-cell over 100 cycles at 0.1C in the voltage range of 1.0–2.4 V vs In/LiIn. The cycling performance of the Se–C–Li_6PS_5Br half-cell is also presented for comparison. The voltage profiles during cycling test and the rate performance of both cells are shown in Figure S16. The initial discharge capacities of the S–C–Li_6PSe_5Br and Se–C–Li_6PS_5Br half-cells are comparable, delivering 5.57 and 5.68 mA h cm^{-2}, respectively. Notably, the capacity retention of S–C–Li_6PSe_5Br half-cell after 100 cycles is 85%, which is higher than the Se–C–Li_6PS_5Br half-cell (28%). The Li–Se SSB formed via the Se – S exchange reaction during ball milling demonstrated good capacity and cycling stability.

4. Conclusion

This work explored distinct sulfur reactions in solid-state Li–S batteries employing two different highly conductive SE. For the solid-state Li–S cell using $Li_{5.5}PS_{4.5}Cl_{1.5}$, an asymmetric redox pathway was revealed at 25 °C. During discharge, sulfur is converted from S_8 to Li_2S_x and then to Li_2S through a two-step reaction, while the reverse conversion from Li_2S to Li_2S_x and from Li_2S_x to S_8 overlap during charge. *Operando* hybrid impedance spectroscopy suggests that elemental S_8, formed at low SOC levels during charge through these overlapping reactions, significantly impedes the charge transport through the CEI and/or the charge transfer at the cathode during charge. In contrast, the discharge intermediate and product, Li_2S_x and Li_2S, hinder electrochemical processes to a lesser extent, owing to differences in conductivities of the reaction products.

For the composite cathode using Li_6PSe_5Br as the catholyte, a selenium composite cathode is formed by the Se – S exchange reaction during planetary ball milling. As Li_6PS_5Br is thermodynamically more stable than Li_6PSe_5Br, ball milling leads to the substitution of selenium in Li_6PSe_5Br by elemental sulfur, resulting in the formation of amorphous selenium, Li_6PS_5Br, and unreacted residual sulfur in the composite cathode. Both selenium and sulfur undergo reversible conversion between their original states and Li_2Se/Li_2S during discharge and charge. Consistent with the S–C–$Li_{5.5}PS_{4.5}Cl_{1.5}$ half-cell, the conversion reaction products influence the electrochemical processes differently depending on their transport properties. The resulting S–C–Li_6PSe_5Br half-cell exhibits a high areal capacity of 5.57 mA h cm^{-2} and good cycling stability (85% after 100 cycles).

Overall, these results provide insights into the role of conversion products in SSB, as well as the potential chemical reactions induced by the ball-milling process and the SE selection. The intrinsic asymmetric sulfur redox pathway and the chalcogen chemistry demonstrated in this study contributes to the development of novel approaches for improving the electrochemical performance of solid-state Li–S batteries.

Data Availability

Data supporting the findings in this study are available at 10.17879/s6zvs-1f068 and are provided through the Universität Münster datastore.

Supporting Information

The Supporting Information is available free of charge at https://pubs.acs.org/doi/xxxxxxxx/xxxxxxx.

- Voltage profile of the C–$Li_{5.5}PS_{4.5}Cl_{1.5}$ half-cell; voltage profile and d*Q*/d*V* plot of the S–C–$Li_{5.5}PS_{4.5}Cl_{1.5}$ half-cell at 0 °C; XAS spectra of reference materials; Overlaid *ex situ* S K-edge XAS spectra of S–C–$Li_{5.5}PS_{4.5}Cl_{1.5}$ cathodes; Raman spectra of carbon-containing composites; 2D DRT mapping of the In | $Li_{5.5}PS_{4.5}Cl_{1.5}$ | In/LiIn cell; 1D DRT and DOP curves of S–C–$Li_{5.5}PS_{4.5}Cl_{1.5}$ and S–C–Li_6PSe_5Br half-cells; 2D DRT mapping of the S–C–$Li_{5.5}PS_{4.5}Cl_{1.5}$ half-cell obtained using the conventional DRT model; Nyquist plots calculated from the 2D DRT-DOP plots for the S–C–$Li_{5.5}PS_{4.5}Cl_{1.5}$ half-cell; comparison of QOCV curves and voltage profiles for the S–C–Li_6PSe_5Br half-cell; Raman spectra of Se powder and ball-milled Se; XRD patterns of the ball-milled S–Li_6PSe_5Br composite before and after annealing; elemental composition of the pristine S–C–Li_6PSe_5Br cathode; GITT curves of the Se–C–$Li_{5.5}PS_{4.5}Cl_{1.5}$ half-cell; voltage profiles and d*Q*/d*V* plots of S–C–Li_6PSe_5Br half-cells at elevated temperatures; XPS spectra of S–C–Li_6PSe_5Br cathodes; 2D DRT-DOP mapping of the Se–C–Li_6PS_5Br half-cell; and voltage profiles and rate performance of Se–C–Li_6PS_5Br and S–C–Li_6PSe_5Br half-cells.

Notes

The authors declare no competing financial interest.

Acknowledgements

This work was financially supported by the German Federal Ministry of Research, Technology, and Space (BMFTR) within the AReLiS-3 project – 13XP0595B. XAS measurements were carried out with the support of Diamond Light Source at beamline B18 under proposal SP41187. We acknowledge that the XPS instrument employed in this work was funded by the German Research Foundation (DFG) – 525733742. J.D.H. further thanks the Alexander von Humboldt Foundation.

References

(1) Busche, M. R.; Adelhelm, P.; Sommer, H.; Schneider, H.; Leitner, K.; Janek, J. Systematical electrochemical study on the parasitic shuttle-effect in lithium-sulfur-cells at different temperatures and different rates. *J. Power Sources* **2014**, *259*, 289–299. DOI: 10.1016/j.jpowsour.2014.02.075.

(2) Ji, X.; Lee, K. T.; Nazar, L. F. A highly ordered nanostructured carbon–sulphur cathode for lithium–sulphur batteries. *Nat. Mater.* **2009**, *8* (6), 500–506. DOI: 10.1038/nmat2460.

(3) Seh, Z. W.; Sun, Y.; Zhang, Q.; Cui, Y. Designing high-energy lithium–sulfur batteries. *Chem. Soc. Rev.* **2016**, *45* (20), 5605–5634. DOI: 10.1039/C5CS00410A.

(4) Manthiram, A.; Chung, S.-H.; Zu, C. Lithium–Sulfur Batteries: Progress and Prospects. *Adv. Mater.* **2015**, *27* (12), 1980–2006. DOI: 10.1002/adma.201405115.

(5) Janek, J.; Zeier, W. G. Challenges in speeding up solid-state battery development. *Nat. Energy* **2023**, *8* (3), 230–240. DOI: 10.1038/s41560-023-01208-9.

(6) Bruce, P. G.; Freunberger, S. A.; Hardwick, L. J.; Tarascon, J.-M. Li–O_2 and Li–S batteries with high energy storage. *Nat. Mater.* **2012**, *11* (1), 19–29. DOI: 10.1038/nmat3191.

(7) Cao, D.; Sun, X.; Li, F.; Bak, S.-M.; Ji, T.; Geiwitz, M.; Burch, K. S.; Du, Y.; Yang, G.; Zhu, H. Understanding Electrochemical Reaction Mechanisms of Sulfur in All-Solid-State Batteries through Operando and Theoretical Studies. *Angew. Chem. Int. Ed.* **2023**, *62* (20), e202302363. DOI: 10.1002/anie.202302363.

(8) Kim, J. T.; Rao, A.; Nie, H.-Y.; Hu, Y.; Li, W.; Zhao, F.; Deng, S.; Hao, X.; Fu, J.; Luo, J.; Duan, H.; Wang, C.; Singh, C. V.; Sun, X. Manipulating Li_2S_2/Li_2S mixed discharge products of all-solid-state lithium sulfur batteries for improved cycle life. *Nat. Commun.* **2023**, *14* (1), 6404. DOI: 10.1038/s41467-023-42109-5.

(9) Gu, J.; Hu, W.; Wu, Y.; Ren, F.; Liang, Z.; Zhong, H.; Zheng, X.; Ma, R.; Luo, Y.; Chen, X.; Shi, J.; Yang, Y. Asymmetric Sulfur Redox Paths in Sulfide-Based All-Solid-State Lithium–Sulfur Batteries. *Chem. Mater.* **2024**, *36* (9), 4403–4416. DOI: 10.1021/acs.chemmater.3c03317.

(10) Ohno, S.; Rosenbach, C.; Dewald, G. F.; Janek, J.; Zeier, W. G. Linking Solid Electrolyte Degradation to Charge Carrier Transport in the Thiophosphate-Based Composite Cathode toward Solid-State Lithium-Sulfur Batteries. *Adv. Funct. Mater.* **2021**, *31* (18), 2010620. DOI: 10.1002/adfm.202010620.

(11) Dewald, G. F.; Ohno, S.; Hering, J. G. C.; Janek, J.; Zeier, W. G. Analysis of Charge Carrier Transport Toward Optimized Cathode Composites for All-Solid-State Liâ□S Batteries. *Batteries & Supercaps* **2021**, *4* (1), 183–194. DOI: 10.1002/batt.202000194.

(12) Whang, G.; Zeier, W. G. Transition Metal Sulfide Conversion: A Promising Approach to Solid-State Batteries. *ACS Energy Lett.* **2023**, *8* (12), 5264–5274. DOI: 10.1021/acsenergylett.3c02246.

(13) Du, L.; Wu, R.; Wu, Z.; Huang, H.; Xia, Y.; Gan, Y.; Zhang, W.; Xia, X.; He, X.; Zhang, J. Research progress of all-solid-state lithium–sulfur batteries with sulfide solid electrolytes: materials, interfaces, challenges, and prospects. *Mater. Chem. Front.* **2023**, *7* (22), 5760–5785. DOI: 10.1039/D3QM00607G.

(14) Ohno, S.; Koerver, R.; Dewald, G.; Rosenbach, C.; Titscher, P.; Steckermeier, D.; Kwade, A.; Janek, J.; Zeier, W. G. Observation of Chemomechanical Failure and the Influence of Cutoff Potentials in All-Solid-State Li–S Batteries. *Chem. Mater.* **2019**, *31* (8), 2930–2940. DOI: 10.1021/acs.chemmater.9b00282.

(15) Tran, Q.-A.; Agrawal, M.; Häusler, M.; Hörmann, J.; Moqadam, M. S.; Redhammer, G. J.; Sellæg Ellingsen, I.; Din, M. M. U.; Vullum, P. E.; Zettl, R.; Danner, T.; Latz, A.; Hennige, V.; Brunner, R.; Rettenwander, D. Uni-Axial Densification of Slurry-Casted Li_6PS_5Cl Tapes: The Role of Particle Size Distribution and Densification Pressure. *Adv. Mater.* **2025**, *37* (30), 2501592. DOI: 10.1002/adma.202501592.

(16) Cronau, M.; Duchardt, M.; Szabo, M.; Roling, B. Ionic Conductivity versus Particle Size of Ball-Milled Sulfide-Based Solid Electrolytes: Strategy Towards Optimized Composite Cathode Performance in All-Solid-State Batteries. *Batteries & Supercaps* **2022**, *5* (6), e202200041. DOI: 10.1002/batt.202200041.

(17) Schweiger, L.; Hogrefe, K.; Gadermaier, B.; Rupp, J. L. M.; Wilkening, H. M. R. Ionic Conductivity of Nanocrystalline and Amorphous $Li_{10}GeP_2S_{12}$: The Detrimental Impact of Local Disorder on Ion Transport. *J. Am. Chem. Soc.* **2022**, *144* (22), 9597–9609. DOI: 10.1021/jacs.1c13477.

(18) Huang, J. D.; Meisel, C.; Sullivan, N. P.; Zakutayev, A.; O'Hayre, R. Rapid mapping of electrochemical processes in energy-conversion devices. *Joule* **2024**, *8* (7), 2049–2072. DOI: 10.1016/j.joule.2024.05.003.

(19) Gautam, A.; Sadowski, M.; Prinz, N.; Eickhoff, H.; Minafra, N.; Ghidiu, M.; Culver, S. P.; Albe, K.; Fässler, T. F.; Zobel, M.; Zeier, W. G. Rapid Crystallization and Kinetic Freezing of Site-Disorder in the Lithium Superionic Argyrodite Li_6PS_5Br. *Chem. Mater.* **2019**, *31* (24), 10178–10185. DOI: 10.1021/acs.chemmater.9b03852.

(20) Zhang, W.; Weber, D. A.; Weigand, H.; Arlt, T.; Manke, I.; Schröder, D.; Koerver, R.; Leichtweiss, T.; Hartmann, P.; Zeier, W. G.; Janek, J. Interfacial Processes and Influence of Composite Cathode Microstructure Controlling the Performance of All-Solid-State Lithium Batteries. *ACS Appl. Mater. Interfaces* **2017**, *9* (21), 17835–17845. DOI: 10.1021/acsami.7b01137.

(21) Ravel, B.; Newville, M. ATHENA, ARTEMIS, HEPHAESTUS: data analysis for X-ray absorption spectroscopy using IFEFFIT. *J. Synchrotron Radiat.* **2005**, *12* (4), 537–541. DOI: 10.1107/S0909049505012719.

(22) Huang, J. D.; Zeier, W. G. Joint-Domain Impedance Spectroscopy for Solid-State Batteries: Enabling Accelerated Characterization and Data-Driven Insights. *ACS Energy Lett.* **2026**, *11*, 986–994. DOI: 10.1021/acsenergylett.5c03055.

(23) Huang, J.; Sullivan, N. P.; Zakutayev, A.; O'Hayre, R. How reliable is distribution of relaxation times (DRT) analysis? A dual regression-classification perspective on DRT estimation, interpretation, and accuracy. *Electrochimica Acta* **2023**, *443*, 141879. DOI: 10.1016/j.electacta.2023.141879.

(24) Li, W.; Seal, S.; Rivero, C.; Lopez, C.; Richardson, K.; Pope, A.; Schulte, A.; Myneni, S.; Jain, H.; Antoine, K.; Miller, A. C. Role of S/Se ratio in chemical bonding of As–S–Se glasses investigated by Raman, x-ray photoelectron, and extended x-ray absorption fine structure spectroscopies. *J. Appl. Phys.* **2005**, *98* (5), 53503. DOI: 10.1063/1.2009815.

(25) Wang, S.; Tang, M.; Zhang, Q.; Li, B.; Ohno, S.; Walther, F.; Pan, R.; Xu, X.; Xin, C.; Zhang, W.; Li, L.; Shen, Y.; Richter, F. H.; Janek, J.; Nan, C.-W. Lithium Argyrodite as Solid Electrolyte and Cathode Precursor for Solid-State Batteries with Long Cycle Life. *Adv. Energy Mater.* **2021**, *11* (31), 2101370. DOI: 10.1002/aenm.202101370.

(26) Tan, Darren H. S.; Wu, E. A.; Nguyen, H.; Chen, Z.; Marple, M. A. T.; Doux, J.-M.; Wang, X.; Yang, H.; Banerjee, A.; Meng, Y. S. Elucidating Reversible Electrochemical Redox of Li_6PS_5Cl Solid Electrolyte. *ACS Energy Lett.* **2019**, *4* (10), 2418–2427. DOI: 10.1021/acsenergylett.9b01693.

(27) Xiao, Y.; Yamamoto, K.; Matsui, Y.; Watanabe, T.; Sakuda, A.; Nakanishi, K.; Uchiyama, T.; Hayashi, A.; Shingubara, S.; Tatsumisago, M.; Ishikawa, M.; Watanabe, M.; Uchimoto, Y. Comparison of Sulfur

Cathode Reactions between a Concentrated Liquid Electrolyte System and a Solid-State Electrolyte System by Soft X-Ray Absorption Spectroscopy. *ACS Appl. Energy Mater.* **2021**, *4* (1), 186–193. DOI: 10.1021/acsaem.0c02063.

(28) Dominko, R.; Patel, M. U. M.; Lapornik, V.; Vizintin, A.; Koželj, M.; N. Tušar, N.; Arčon, I.; Stievano, L.; Aquilanti, G. Analytical Detection of Polysulfides in the Presence of Adsorption Additives by Operando X-ray Absorption Spectroscopy. *J. Phys. Chem. C* **2015**, *119* (33), 19001–19010. DOI: 10.1021/acs.jpcc.5b05609.

(29) Patel, M. U. M.; Arčon, I.; Aquilanti, G.; Stievano, L.; Mali, G.; Dominko, R. X-ray Absorption Near-Edge Structure and Nuclear Magnetic Resonance Study of the Lithium–Sulfur Battery and its Components. *ChemPhysChem* **2014**, *15* (5), 894–904. DOI: 10.1002/cphc.201300972.

(30) Whang, G.; Huang, J.; Le Pham, P. N.; Kraft, M. A.; Zeier, W. G. Not All Lithium–Indium Counter Electrodes Are Made Equal: Probing the Inhomogeneities and Kinetics of Uniaxially Pressed Li–In Counter Electrodes in All Solid-State Batteries. *ACS Electrochem.* **2025**, *1* (2), 249–262. DOI: 10.1021/acselectrochem.4c00060.

(31) Lu, P.; Wu, Y.; Wu, D.; Song, F.; Ma, T.; Yan, W.; Zhu, X.; Guo, F.; Lu, J.; Peng, J.; Chen, L.; Li, H.; Wu, F. Rate-limiting mechanism of all-solid-state battery unravelled by low-temperature test-analysis flow. *Energy Stor. Mater.* **2024**, *67*, 103316. DOI: 10.1016/j.ensm.2024.103316.

(32) Yu, C.-Y.; Choi, J.; Dunham, J.; Ghahremani, R.; Liu, K.; Lindemann, P.; Garver, Z.; Barchiesi, D.; Farahati, R.; Kim, J.-H. Time-resolved impedance spectroscopy analysis of aging in sulfide-based all-solid-state battery full-cells using distribution of relaxation times technique. *J. Power Sources* **2024**, *597*, 234116. DOI: 10.1016/j.jpowsour.2024.234116.

(33) Soni, R.; Robinson, J. B.; Shearing, P. R.; Brett, D. J.; Rettie, A. J.; Miller, T. S. Lithium-sulfur battery diagnostics through distribution of relaxation times analysis. *Energy Stor. Mater.* **2022**, *51*, 97–107. DOI: 10.1016/j.ensm.2022.06.016.

(34) Truong, T. K.; Whang, G.; Huang, J.; Sandoval, S. E.; Zeier, W. G. Probing solid-state battery aging: evaluating calendar vs. cycle aging protocols via time-resolved electrochemical impedance spectroscopy. *J. Mater. Chem. A* **2025**, *13* (23), 17261–17270. DOI: 10.1039/D5TA01083G.

(35) Hakari, T.; Hayashi, A.; Tatsumisago, M. Li_2S-Based Solid Solutions as Positive Electrodes with Full Utilization and Superlong Cycle Life in All-Solid-State Li/S Batteries. *Adv. Sustain. Syst.* **2017**, *1* (6), 1700017. DOI: 10.1002/adsu.201700017.

(36) Han, F.; Yue, J.; Fan, X.; Gao, T.; Luo, C.; Ma, Z.; Suo, L.; Wang, C. High-Performance All-Solid-State Lithium–Sulfur Battery Enabled by a Mixed-Conductive Li_2S Nanocomposite. *Nano Lett.* **2016**, *16* (7), 4521–4527. DOI: 10.1021/acs.nanolett.6b01754.

(37) Alt, C. D.; Kessler-Kühn, J.; Eckhardt, J. K.; Stein, M.; Chatterjee, S.; Elm, M. T.; Janek, J. The partial electronic conductivity of lithium halides and their role in SEI formation in solid-state batteries – Hebb-Wagner-type measurements. *Solid State Ionics* **2025**, *429*, 116991. DOI: 10.1016/j.ssi.2025.116991.

(38) Song, H.; Münch, K.; Liu, X.; Shen, K.; Zhang, R.; Weintraut, T.; Yusim, Y.; Jiang, D.; Hong, X.; Meng, J.; Liu, Y.; He, M.; Li, Y.; Henkel, P.; Brezesinski, T.; Janek, J.; Pang, Q. All-solid-state Li–S batteries with fast solid–solid sulfur reaction. *Nature* **2025**, *637* (8047), 846–853. DOI: 10.1038/s41586-024-08298-9.

(39) Wang, L.; Yin, X.; Li, B.; Zheng, G. W. Mixed Ionically/Electronically Conductive Double-Phase Interface Enhanced Solid-State Charge Transfer for a High-Performance All-Solid-State Li–S Battery. *Nano Lett.* **2022**, *22* (1), 433–440. DOI: 10.1021/acs.nanolett.1c04228.

(40) Wang, D.; Gwalani, B.; Wierzbicki, D.; Singh, V.; Jhang, L.-J.; Rojas, T.; Kou, R.; Liao, M.; Ye, L.; Jiang, H.; Shan, S.; Silver, A.; Ngo, A. T.; Du, Y.; Li, X.; Wang, D. Overcoming the conversion reaction limitation at three-phase interfaces using mixed conductors towards energy-dense solid-state Li–S batteries. *Nat. Mater.* **2025**, *24* (2), 243–251. DOI: 10.1038/s41563-024-02057-x.

(41) Hartel, J.; Banik, A.; Gerdes, J. M.; Wankmiller, B.; Helm, B.; Li, C.; Kraft, M. A.; Hansen, M. R.; Zeier, W. G. Understanding Lithium-Ion Transport in Selenophosphate-Based Lithium Argyrodites and Their Limitations in Solid-State Batteries. *Chem. Mater.* **2023**, *35* (12), 4798–4809. DOI: 10.1021/acs.chemmater.3c00658.

(42) Schlem, R.; Ghidiu, M.; Culver, S. P.; Hansen, A.-L.; Zeier, W. G. Changing the Static and Dynamic Lattice Effects for the Improvement of the Ionic Transport Properties within the Argyrodite $Li_6PS_{5-x}Se_xI$. *ACS Appl. Energy Mater.* **2020**, *3* (1), 9–18. DOI: 10.1021/acsaem.9b01794.

(43) Goldan, A. H.; Li, C.; Pennycook, S. J.; Schneider, J.; Blom, A.; Zhao, W. Molecular structure of vapor-deposited amorphous selenium. *J. Appl. Phys.* **2016**, *120* (13), 135101. DOI: 10.1063/1.4962315.

(44) Shen, K.; Shi, W.; Song, H.; Zheng, C.; Yan, Y.; Hong, X.; Liu, X.; An, Y.; Li, Y.; Ye, F.; He, M.; Ye, G.; Ma, C.; Zheng, L.; Gao, P.; Pang, Q. Solid Catholyte with Regulated Interphase Redox for All-Solid-State Lithium-Sulfur Batteries. *Adv. Mater.* **2025**, *37* (11), 2417171. DOI: 10.1002/adma.202417171.

(45) Shannon, R. Revised effective ionic radii and systematic studies of interatomic distances in halides and chalcogenides. *Acta Cryst. A* **1976**, *32* (5), 751–767.

(46) Pauling, L. The nature of the chemical bond. IV. The energy of single bonds and the relative electronegativity of atoms. *J. Am. Chem. Soc.* **1932**, *54* (9), 3570–3582.

(47) Saal, J. E.; Kirklin, S.; Aykol, M.; Meredig, B.; Wolverton, C. Materials Design and Discovery with High-Throughput Density Functional Theory: The Open Quantum Materials Database (OQMD). *JOM* **2013**, *65* (11), 1501–1509. DOI: 10.1007/s11837-013-0755-4.

(48) Kirklin, S.; Saal, J. E.; Meredig, B.; Thompson, A.; Doak, J. W.; Aykol, M.; Rühl, S.; Wolverton, C. The Open Quantum Materials Database (OQMD): assessing the accuracy of DFT formation energies. *npj Comput. Mater.* **2015**, *1* (1), 15010. DOI: 10.1038/npjcompumats.2015.10.

(49) Jain, A.; Ong, S. P.; Hautier, G.; Chen, W.; Richards, W. D.; Dacek, S.; Cholia, S.; Gunter, D.; Skinner, D.; Ceder, G.; Persson, K. A. Commentary: The Materials Project: A materials genome approach to accelerating materials innovation. *APL Mater.* **2013**, *1* (1), 11002. DOI: 10.1063/1.4812323.

(50) Walther, F.; Randau, S.; Schneider, Y.; Sann, J.; Rohnke, M.; Richter, F. H.; Zeier, W. G.; Janek, J. Influence of Carbon Additives on the Decomposition Pathways in Cathodes of Lithium Thiophosphate-Based All-Solid-State Batteries. *Chem. Mater.* **2020**, *32* (14), 6123–6136. DOI: 10.1021/acs.chemmater.0c01825.

(51) Walther, F.; Strauss, F.; Wu, X.; Mogwitz, B.; Hertle, J.; Sann, J.; Rohnke, M.; Brezesinski, T.; Janek, J. The Working Principle of a Li_2CO_3/$LiNbO_3$ Coating on NCM for Thiophosphate-Based All-Solid-State Batteries. *Chem. Mater.* **2021**, *33* (6), 2110–2125. DOI: 10.1021/acs.chemmater.0c04660.

(52) Walther, F.; Koerver, R.; Fuchs, T.; Ohno, S.; Sann, J.; Rohnke, M.; Zeier, W. G.; Janek, J. Visualization of the Interfacial Decomposition of Composite Cathodes in Argyrodite-Based All-Solid-State Batteries Using Time-of-Flight Secondary-Ion Mass Spectrometry. *Chem. Mater.* **2019**, *31* (10), 3745–3755. DOI: 10.1021/acs.chemmater.9b00770.

(53) Auvergniot, J.; Cassel, A.; Ledeuil, J.-B.; Viallet, V.; Seznec, V.; Dedryvère, R. Interface Stability of Argyrodite Li_6PS_5Cl toward $LiCoO_2$, $LiNi_{1/3}Co_{1/3}Mn_{1/3}O_2$, and $LiMn_2O_4$ in Bulk All-Solid-State Batteries. *Chem. Mater.* **2017**, *29* (9), 3883–3890. DOI: 10.1021/acs.chemmater.6b04990.

(54) Fan, H.-N.; Chen, S.-L.; Chen, X.-H.; Tang, Q.-L.; Hu, A.-P.; Luo, W.-B.; Liu, H.-K.; Dou, S.-X. 3D Selenium Sulfide@Carbon Nanotube Array as Long-Life and High-Rate Cathode Material for Lithium Storage. *Adv. Funct. Mater.* **2018**, *28* (43), 1805018. DOI: 10.1002/adfm.201805018.

(55) Eithiraj, R. D.; Jaiganesh, G.; Kalpana, G.; Rajagopalan, M. First-principles study of electronic structure and ground-state properties of alkali-metal sulfides – Li_2S, Na_2S, K_2S and Rb_2S. *Phys. Status Solidi B* **2007**, *244* (4), 1337–1346. DOI: 10.1002/pssb.200642506.

(56) Eithiraj, R. D.; Jaiganesh, G.; Kalpana, G. FIRST-PRINCIPLES STUDY OF ELECTRONIC STRUCTURE AND GROUND-STATE PROPERTIES OF ALKALI-METAL SELENIDES AND TELLURIDES (M_2A)[M: Li, Na, K; A: Se, Te]. *Int. J. Mod. Phys. B* **2009**, *23* (25), 5027–5037. DOI: 10.1142/S0217979209052418.

(57) Koyama, Y.; Yamada, Y.; Tanaka, I.; Nishitani, S.; R.; Adachi, H.; Murayama, M.; Kanno, R. Evaluation of Migration Energy of Lithium Ions in Chalcogenides and Halides by First Principles Calculation. *Mater. Trans.* **2002**, *43* (7), 1460–1463. DOI: 10.2320/matertrans.43.1460.

(58) Lee, J. T.; Kim, H.; Oschatz, M.; Lee, D.-C.; Wu, F.; Lin, H.-T.; Zdyrko, B.; Cho, W. I.; Kaskel, S.; Yushin, G. Micro- and Mesoporous Carbide-Derived Carbon–Selenium Cathodes for High-Performance Lithium Selenium Batteries. *Adv. Energy Mater.* **2015**, *5* (1), 1400981. DOI: 10.1002/aenm.201400981.

(59) Xu, G.-L.; Sun, H.; Luo, C.; Estevez, L.; Zhuang, M.; Gao, H.; Amine, R.; Wang, H.; Zhang, X.; Sun, C.-J.; Liu, Y.; Ren, Y.; Heald, S. M.; Wang, C.; Chen, Z.; Amine, K. Solid-State Lithium/Selenium–Sulfur Chemistry Enabled via a Robust Solid-Electrolyte Interphase. *Adv. Energy Mater.* **2019**, *9* (2), 1802235. DOI: 10.1002/aenm.201802235.

TOC Graphic

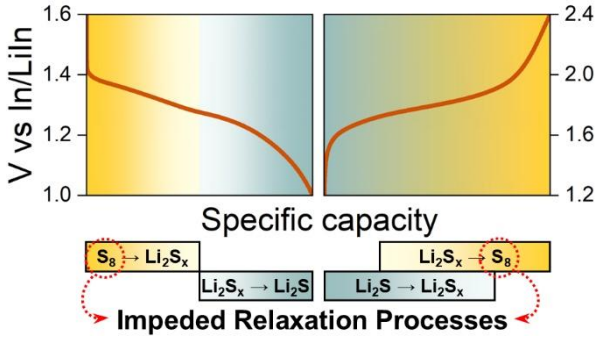
V vs In/LiIn
1.6
1.4
1.2
1.0
2.4
2.0
1.6
1.2
Specific capacity
S8 → Li2Sx
Li2Sx → Li2S
Li2Sx → S8
Li2S → Li2Sx
Impeded Relaxation Processes